# A Comprehensive Experimental Investigation of Hydraulically Supported Robot Assisted Incremental Sheet Forming of Al6061 Sheets

Ravi Prakash Singh[a,b,c,*], Santosh Kumar[c], Edward Brambley[a,b], Pankaj Kumar Singh[d], Karthik Gangaraju[c]

[a] *WMG, University of Warwick, Coventry, CV4 7AL, UK*
[b] *Mathematics Institute, University of Warwick, Coventry, CV4 7AL, UK*
[c] *Department of Mechanical Engineering, Indian Institute of Technology, Varanasi, 221005, India*
[d] *Department of Mechanical Engineering, Poornima University, Jaipur, 303905, India*

Published in ASME Journal of Manufacturing Science and Engineering, volume 148, 011001 (2026),
doi:10.1115/1.4070137

---

## Abstract

In the current study, robot assisted incremental sheet forming (RAISF) was performed on 1.05 mm thick sheets of aluminium alloy 6061 (AA6061), which was supported from underneath by fluid; this process is named robot assisted incremental sheet hydroforming (RAISHF). A variable wall angle conical frustum (VWACF) was fabricated, both with and without the fluid support. The cone formed by RAISHF was 6.67% steeper and 28.47% deeper than with RAISF alone. Spring back was reduced by 77.14%, suggesting better accuracy of the formed part. The role of fluid pressure in enhancing the performance of RAISHF was explained by considering a through thickness element under equilibrium conditions. For cones of identical wall angle formed with RAISF and RAISHF, the thickness distribution, tensile properties, microhardness, major and minor strains in the plane of the sheet, microstructure, and residual stresses were characterized, with RAISHF exhibiting more uniform thickness distribution, more even strain distribution, and less hardening. X-Ray diffraction revealed the residual stress on the surface of the cone in both processes to be tensile, with RAISHF showing lower residual stress. Microstructure of the samples taken from formed cones revealed that, due to dynamic recrystallization, more strain can be obtained by RAISHF.

*Keywords:* Incremental forming, Hydroforming, Straight groove test, Nakajima test, Forming limit

---

## 1. Introduction

Incremental sheet forming (ISF) is an advanced manufacturing process that does not involve use of dedicated dies for sheet forming and is used for small batch production of complex three-dimensional shapes [1]. ISF has been an area of interest among researchers and industry alike due to its various advantages over conventional stamping and deep-drawing processes [2]. Emmens and van den Boogaard [3] demonstrated that strains in ISF exceed the forming limit curve (FLC) of conventional processes like deep drawing and stamping. The improvement in formability in ISF is attributed to localized deformation, creating high level of compressive stresses that suppress voids and delay necking. They identified factors such as contact stress, bending under tension, shear, cyclic strain, and hydrostatic stress as key contributors to improved formability in ISF. Several studies have been reported on studying formability in ISF process using Straight groove test [2] and Variable Wall Angle Conical Frustum (VWACF) [4].In the early stages of ISF development, the process was carried out on a 5/6-axis CNC machine. However, more recently, industrial robotic arms have been employed to carry out ISF, leading to the emergence of Robot-Assisted Incremental Sheet Forming (RAISF), also known as Roboforming [5]. Robotic arms offer advantages such as improved speed control, accuracy, payload capacity, and workspace, enabling the fabrication of large and complex three dimensional shapes [6]. Additionally, in recent times, some other changes have also been made in ISF to enhance the capabilities of the process. Some of these are hot/warm ISF using induction heating [7–9] Laser-Assisted heating [10, 11], and ISF with ultrasonic vibrations [12, 13].

One of the major limitations of ISF is geometrical inaccuracy of the formed product [14, 15]. Hirt et al. [16] presented a comprehensive review of the geometrical inaccuracies occurring during ISF. It was reported that the geometrical inaccuracies arising in the products formed by ISF is primarily due to plastic deformation outside the contact zone, elastic deflection, spring back due to release of the regular elastic part of the local deformation and induced residual stresses.The absence of die in the area underneath the sheet and the retained elasticity in the sheet further exacerbate spring back, which negatively impacts the surface finish of the formed product [17, 18].

---

[*] Corresponding Author
*Email address:* `ravi.p.singh@warwick.ac.uk` (Ravi Prakash Singh)

To overcome this limitation, researchers have proposed various strategies, such as using partial dies on the backside of the sheet to provide localized support during forming [19], and utilizing flexible media that act as pseudo-dies to improve the geometric accuracy of the formed product [20]. The use of pressurized fluid has been explored extensively by the researchers primarily in hydromechanical deep drawing due to its advantages and the process is loosely termed as Sheet Hydroforming (SHF)[21]. In SHF, the fluid's flexible nature allows it to act as a die, forming sheet metals into complex geometries [22, 23]. This process offers several advantages over conventional deep drawing. The hydrostatic nature of fluid pressure ensures uniform load application, which significantly reduces localized thinning [24]. Additionally, the reduction of through-thickness stress gradients [25] minimizes stress concentrations, thus delaying necking and improving formability [26]. Furthermore, reduced springback has also been reported by Sun and Lang [27], leading to higher accuracy and precision in the formed parts. Similarly, the use of flexible mediums in ISF can introduce a hydrostatic pressure component that can significantly improve the process potentially due to pressure induced ductility [28, 29] and altering stress state, leading to uniform strain distribution throughout the formed component [30]. The reported flexible mediums are pressurized air[31], metallic foam [32], rubber [33] and static fluid [34]. McLoughlin et al. [31] applied pressurized air from the back of the sheet at 0.0035 bar and observed no significant change in the geometrical accuracy of the formed parts. Khalifa and Thiery [35] used gas as an active medium from back side of the sheet, which acted as a supplementary tool, and under controlled pressure, a concave-convex shape was formed. They also studied two-stage incremental sheet forming with an active medium and ***it*** was reported that accuracy in formed product was improved compared to single-stage forming. The convex preform height of 75% of the target height, significantly reduced flange bending due to decrease in vertical forces [36]. Similar trends in vertical forces were observed by Zimeng et al. [37] while performing FEA of ISF with isostatic pressing from back. Shang et al. [38, 39] used finite element modeling to study ISF with hydraulic support Shang et al. [38, 39] and validated their results through experiments, finding a significant improvement in the uniformity of thickness distribution in the formed product. The wall angle of the formed cone was also improved with the use of hydraulic support, as reported by Kumar and Kumar [40], who developed an Incremental Sheet Hydroforming (ISHF) setup by introducing hydraulic fluid from the backside of the sheet to deform aluminium sheets. Using FEA modeling with Deform 3D, they observed that ISHF required lower forming forces due to increased material ductility compared to ISF. They further employed multi-stage ISHF to achieve wall angles as high as 90° to form near vertical frustums [20].

It can be understood from the above discussion that ISHF can be a more capable process as compared to the conventional ISF. While several studies have explored incremental sheet forming and hydromechanical deep drawing, limited research has been conducted on ISHF. The aim of the current work is to broadly compare the processes of ISF and ISHF performed on six axes of industrial robot. Robot-Assisted Incremental Sheet Forming (RAISF) and Robot-Assisted Incremental Sheet Hydroforming (RAISHF) processes were employed to form various shapes using sheets of AA6061. Conical frustums were formed using parameters optimized by straight groove tests. The outputs of both RAISF and RAISHF were analyzed and compared across several aspects, including formability and strain-strain space (section 5.1), thickness distribution, accuracy of the formed product (section 5.2), mechanical properties such as strength and microhardness (section 5.3), residual stresses (section 5.4), and microstructural evolution (section 5.5). The mechanics of RAISHF (section 3) was developed by analyzing a through-thickness element, providing a theoretical model to study the improved formability and reduced springback.

## 2. Experimental setup and robotic tool path planning

The experimental setup for RAISF and RAISHF as shown in Figure 1 was established from scratch in the Production lab facility at IIT (BHU) and was patented with title of Invention "Robot Assisted High Speed Incremental Sheet Hydroforming Machine". The setup and its working has been described comprehensively in the previous works undertaken by the authors [9, 41, 42]. It consists of the main parts which are: a six-axis industrial robot a having a payload of 180 kN with a controller and teach pendant, clamping arrangement, forming tool, tool dynamometer for force measurement, fluid chamber (only used for RAISHF),piston and cylinder assembly to maintain hydraulic pressure, control valves $(V_1, V_2, V_3)$, pressure sensors and gauge for pressure monitoring. Various parts of the setup have been shown in Figure 1. To avoid any air and fluid leakage from the fluid chamber, silica gel and epoxy rubber was used between the flange and the fluid chamber. The working methodology of RAISHF can be understood from Figure 2(a). The sheet was clamped between the flanges and was sealed with silica gel and epoxy rubber to make it leak free and airtight. The fluid chamber was made oil full prior to forming. Valves $V_1$ and $V_2$ were closed and $V_3$ was open. Fluid pressure from the back of the sheet was maintained by using piston-cylinder arrangement with a counter weight. It was found that a high pressure ($>$ 1.3 bar), caused bulge in the sheet in the upward direction, and subsequent forming by the tool in the downward direction caused folds and crack in the formed cone as shown in the Figure 2 (b). Hence a pressure in the range of $1.0 - 1.3$ bar was

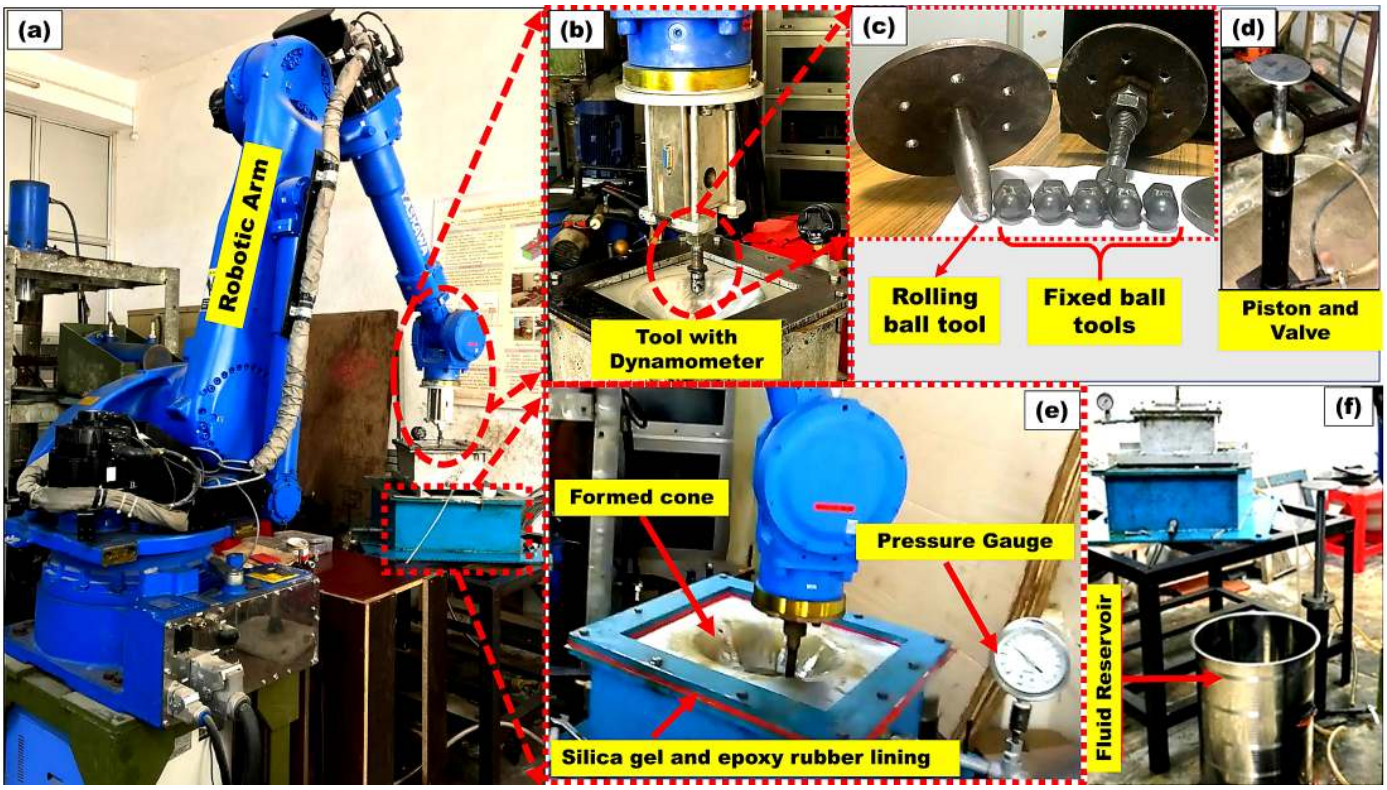

Figure 1: Robot assisted incremental sheet hydroforming setup: (a) labelled diagram of existing setup, (b) forming tool and formed sheet (c) Various tool used for forming, (d) piston and valve arrangement, (e) fluid chamber with sealing (f) fluid chamber.

chosen. This pressure was maintained simply by piston-cylinder arrangement, and naturally was not sufficient for causing any significant plastic deformation, but to act as a support and a flexible die from the back of the sheet to ensure better geometrical accuracy of the formed product and uniform strain distribution. Similar recommendations have been given by Shang et al. [38, 39]. The cone formed and the pressure generated during the formation of the cone has been shown in Figure 2 (c) and (d) respectively. Once the forming was complete Valve $V_1$ was opened to put fluid back to the reservoir.

For tool path planning, couple of methods were adopted.

1. ***Teach pendant based tool path planning:*** In this method, in situ tool path planning was carried out with a teach pendant. This planning was adopted for fabricating both axis-symmetric and non-axis-symmetric shapes with fixed wall angles. The process is explained further through a sample program that generates an axis-symmetric cone, as shown in Figure 3(a). The process is fast and works efficiently particularly for simple geometries with fixed wall angles.
2. ***Software based tool path planning:*** However, in scenarios involving more intricate shapes, such as those with varying wall angles, the use of the teach pendant for tool path planning becomes less practical as number of points to be specified becomes impractically high. In such instances, a software-based tool path planning strategy was implemented. In this strategy shapes and corresponding tool paths, once generated on 3D modelling software (CATIAV5 in current study) was converted into.stl file to get the information of each layer separated by vertical step depth ($\Delta$Z). NC file was obtained from .stl file which can be directly fed into the RobotDK software which serves as an intermediary, establishing an interface between the robotic system and computer-based planning. The process for software based strategy is shown in 3(b).

The fixed ball tool was used in the current study, as it gives rise to a kinetic friction condition, leading to more localized heating which can induce softening effect to the sheet and leading to higher degree of deformation. The experimental parameters of tool speed, tool diameter, and step depth were selected using straight groove test due to its simplicity and rapid execution. The optimal parameter values determined were a tool speed of 85 mm/s, a step size of 0.4 mm, and a tool diameter of 12.5 mm, resulting in a composite desirability of 0.7652. These parameters were chosen for further experimentation.

## 3. Mechanics of RAISHF

For understanding the underlying mechanics behind RAISHF, a through thickness element was taken and is

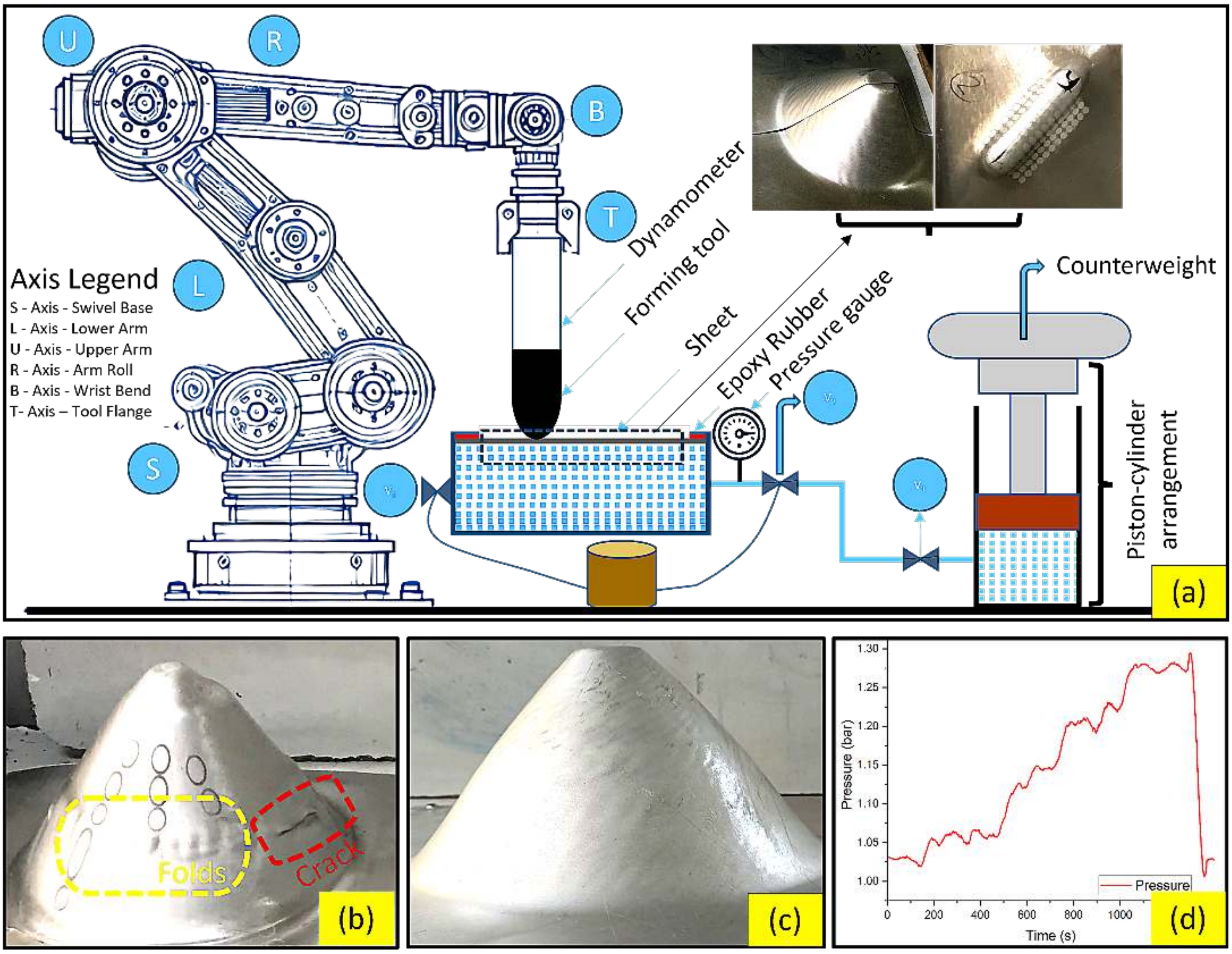

Figure 2: Representation of RAISHF: (a)Schematic diagram for working of RAISHF (b) Crack and fold in the sample when formed with a high back pressure (c) successfully formed cone and (d) Pressure from back during successful formation of cone

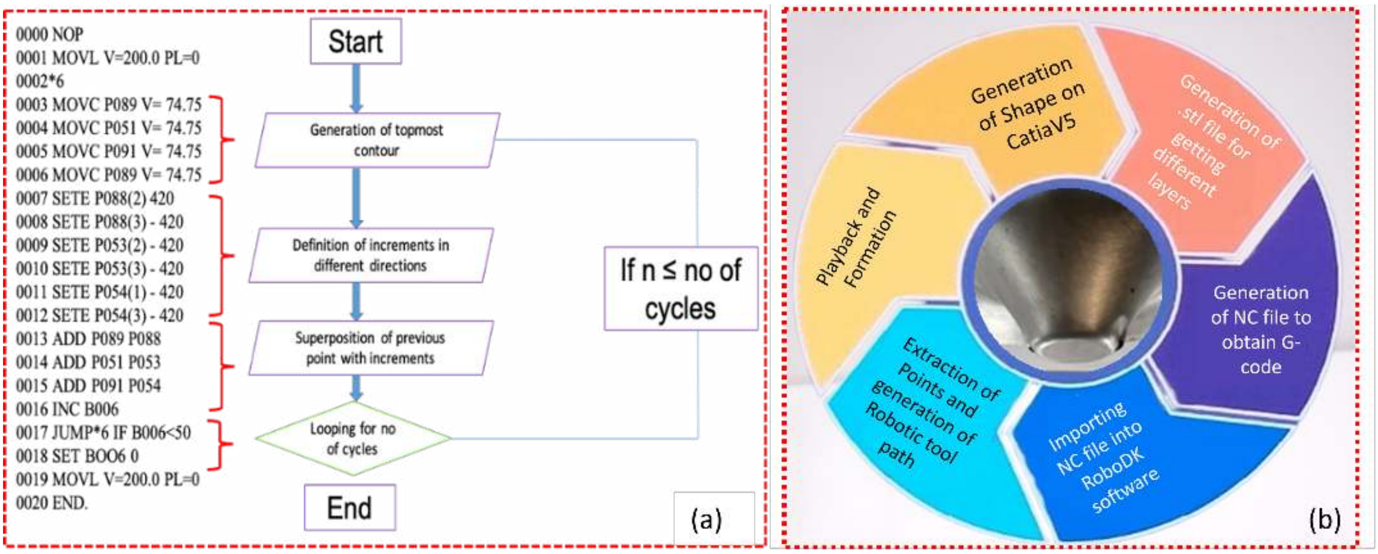

```
0000 NOP
0001 MOVL V=200.0 PL=0
0002*6
0003 MOVC P089 V= 74.75
0004 MOVC P051 V= 74.75
0005 MOVC P091 V= 74.75
0006 MOVC P089 V= 74.75
0007 SETE P088(2) 420
0008 SETE P088(3) - 420
0009 SETE P053(2) - 420
0010 SETE P053(3) - 420
0011 SETE P054(1) - 420
0012 SETE P054(3) - 420
0013 ADD P089 P088
0014 ADD P051 P053
0015 ADD P091 P054
0016 INC B006
0017 JUMP*6 IF B006<50
0018 SET BOO6 0
0019 MOVL V=200.0 PL=0
0020 END.
```

Figure 3: Various tool path strategies: (a) Sample tool path program on teach pendant (b) software-based tool path strategy for VWACF

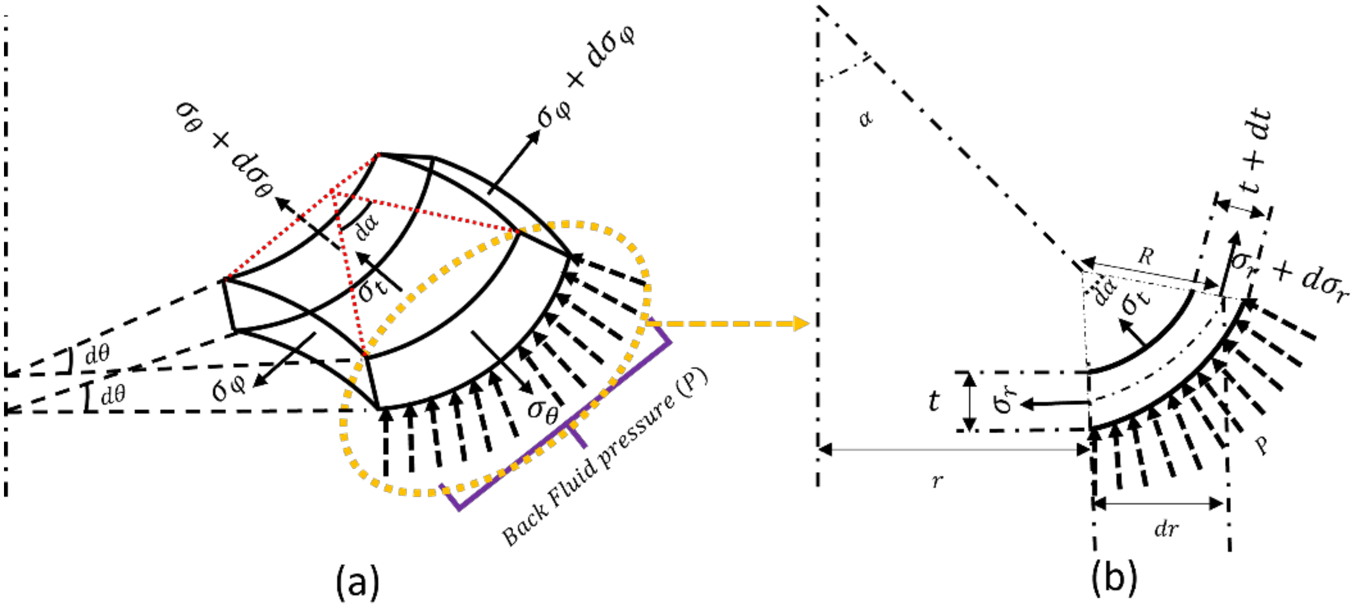

Figure 4: Equillibrium of stresses in Through thickness element : (a) 3D Isometric View (b) Front view

shown in Figure 4 from the region of tool sheet contact with stresses in thickness (t), circumferential ($\theta$) and meridional ($\phi$) directions. The equilibrium equation in the thickness direction can be written as:

$$\begin{aligned}\sigma_t r \mathrm{d}\theta R \mathrm{d}\alpha - \sigma_\phi r \mathrm{d}\theta t \frac{\sin \mathrm{d}\alpha}{2} \\ - (\sigma_\phi + \mathrm{d}\sigma_\phi)(r + \mathrm{d}r)\mathrm{d}\theta(t + \mathrm{d}t)\frac{\sin \mathrm{d}\alpha}{2} \\ - P\left(R + t + \frac{\mathrm{d}t}{2}\right)\mathrm{d}\alpha\left(r + \frac{\mathrm{d}r}{2}\right)\mathrm{d}\theta = 0\end{aligned} \tag{1}$$

Neglecting the higher order terms and treating $d\alpha$ as small, gives the final equation as:

$$\frac{\sigma_t - P}{t} = \frac{\sigma_\phi + P}{R} \tag{2}$$

In absence of fluid from the back, equation (2) simply converges:

$$\frac{\sigma_t}{t} = \frac{\sigma_\phi}{R} \tag{3}$$

Comparing equation (2) and (3), it can be concluded that, the effective compressive stress in the thickness direction is decreasing and that in the meridional direction is increasing by an amount equal to the fluid pressure. This immediately shows that there is a delocalization of thickness stress to the meridional direction by the application of fluid pressure which ensures a more uniform stress distribution also leading to more uniform strain distribution.

It should also be noted that, the excessive fluid pressure from the back can actually aggravate the level of meridional stress which can lead to premature tensile fracture due to shifting the Mohr circle in the Tensile region as reported by Silva et al. [43].It is in accordance with the experimental observations which led the authors to choose the pressure range between 1.0-1.3 bars. As per Jeswiet et al. [44] and Filice et al. [45], under plain strain condition the strain in circumferential direction ($\epsilon_\theta$) can be neglected, which makes the stress in circumferential direction as:

$$\sigma_\theta = \frac{1}{2}(\sigma_t + \sigma_\phi) \tag{4}$$

The complete state of stress for the through thickness element can be given as:

$$\sigma'_t = \sigma_t - P \quad \text{(Compressive)} \tag{5a}$$

$$\sigma'_\phi = \sigma_\phi + P \quad \text{(Tensile)} \tag{5b}$$

$$\sigma'_\theta = \sigma_\theta \quad \text{(Tensile)} \tag{5c}$$

where primed stresses represent the stress state in RAISHF, while the non-primed stresses correspond to the stresses in conventional RAISF. It is evident that the introduction of fluid pressure in RAISHF increases the level of hydrostatic stress. This elevated hydrostatic stress suppresses void nucleation and growth, thereby delaying the onset of fracture, as established by Gurson [46] and Tvergaard and Needleman [47]. Consequently, the application of fluid pressure from the backside of the sheet enhances the material's formability by mitigating fracture initiation. Furthermore, the improved hydrostatic stress promotes more uniform strain distribution, resulting in greater geometrical accuracy of the formed product and reduced springback.

Table 1: Composition and Mechanical Properties of AA6061 Aluminium Alloy

<table>
<tr><th colspan="10">Composition (wt.%)</th></tr>
<tr><td>Elements</td><td>Al</td><td>Ti</td><td>Si</td><td>Mg</td><td>Fe</td><td>Mn</td><td>Zn</td><td>Cr</td><td>Cu</td></tr>
<tr><td>wt.%</td><td>97.41</td><td>0.05</td><td>0.54</td><td>0.82</td><td>0.41</td><td>0.02</td><td>0.06</td><td>0.15</td><td>0.35</td></tr>
<tr><th colspan="10">Mechanical Properties</th></tr>
<tr><th colspan="2">Tensile Properties</th><th colspan="8">Erichsen Ductility (Dome Height $H_D$)</th></tr>
<tr><td>Property</td><td>Value</td><td>Dome 1</td><td>Dome 2</td><td>Dome 3</td><td colspan="5"></td></tr>
<tr><td>Yield Strength (MPa)</td><td>112 ± 5</td><td>IE (mm)</td><td>9.34</td><td>9.12</td><td>8.92</td><td colspan="4"></td></tr>
<tr><td>UTS (MPa)</td><td>127 ± 5</td><td>$H_D$ (mm)</td><td>9.02</td><td>8.82</td><td>8.61</td><td colspan="4">Average $H_D = 9.13$</td></tr>
<tr><td>Elongation (%)</td><td>12.16 ± 0.1</td><td colspan="8"></td></tr>
<tr><th colspan="10">Experimental Details</th></tr>
<tr><th colspan="2">Experimental Parameters</th><th colspan="8">Details of VWACF Fabricated by RAISF and RAISHF</th></tr>
<tr><td>Parameters</td><td>Value</td><td>Process</td><td>$\theta_i (^\circ)$</td><td>$\theta_f$ $(^\circ)$</td><td colspan="2">Theoretical Depth</td><td colspan="3">Actual Depth</td></tr>
<tr><td>Tool Speed</td><td>80 mm/s</td><td>RAISF</td><td>30</td><td>60</td><td colspan="2">36.60</td><td colspan="3">32.42</td></tr>
<tr><td>Tool Diameter</td><td>12.5 mm</td><td>RAISHF</td><td>30</td><td>64</td><td colspan="2">42.76</td><td colspan="3">41.65</td></tr>
<tr><td>Step Depth ($\Delta Z$)</td><td>0.4 mm</td><td colspan="8"></td></tr>
</table>

## 4. Base Material

For this work, sheets of AA6061 of 1.05 mm thickness were used, as this grade of alumunium is widely used in sheet metal industries. The alloy AA6061 was solution heat-treated for 2 hours at 415 $^\circ C$ to achieve the homogenized phases and then furnace-cooled to 260 $^\circ C$ and held for one hour, and finally air cooled [48].

The composition of the AA6061 was determined by optical emission spectrometer and is presented in Table 1. To assess the mechanical properties of the sheet before forming, tensile test, Erichsen ductility test and Nakajima test was performed.The uniaxial tensile test was performed on a 100 kN INSTRON (MODEL 8801) using samples as per the ASTM/E8 standard. For studying the formability of the AA6061 sheet after heat treatment, Erichsen ductility test was conducted. The specimens were prepared as per $ASTM/E643/15$ standard. The diameter of indenter was 20 mm with main scale division 1 mm, and the circular scale division of $50/5MSD$. Three domes were formed by the indenter, just until the onset of fracture of the dome, and the depth of the indentation was measured as ($H_D$). The tensile properties and the details of the depth of indentation ($H_D$) of all the domes formed is presented in Table 1. The formability of the preform material after heat treatment was evaluated comprehensively using the forming limit curve (FLC), plotted as per the ISO 12004-2: 2008 standard [49] via the Nakajima test. The test was conducted on an ITC Interlaken 1000 kN hydraulic press equipped with a Nakajima punch and a smooth clamp ring set [50]. A hemispherical punch with a 100 mm diameter was used to perform out-of-plane stretching on a series of sample geometries, generating different strain paths, as shown in Figure 5.

The sample in Figure 5(a) generates an equi-biaxial strain path, while the sample in Figure 5(g) generates a uniaxial strain path. The samples in between produce other strain paths, ranging between these two extremes, including biaxial and plane strain paths. Figure 5 (h) shows the orientation of the specimen geometries during the tests. The tests were conducted at a constant punch speed of 1 mm/s directly affecting the strain rate, the calculation for which has been included in Appendix A . For a specimen width of 40 mm, the strain rate was found to be $0.0063\,s^{-1}$, which was the maximum observed during the test. In contrast, for the biaxial strain path, where the specimen width was 178 mm, the 100 mm diameter punch deformed the specimen at a strain rate of $0.0019\,s^{-1}$, the lowest recorded in the experiment. A minimum of three repeats were carried out for each sample geometry. Friction was minimized on the punch by applying a lubrication stack (tallow/Teflon/tallow/PVC/tallow/Teflon/tallow layers) between the specimen and the punch. The failure strain was measured with a GOM 5M digital image correlation (DIC) system using a position-dependent method. The DIC system consisted of two 5MP cameras fitted with 50 mm lenses to capture images of the sample surface at a frame rate of 20 frames per second. A speckled paint pattern was applied to the sample surface before the

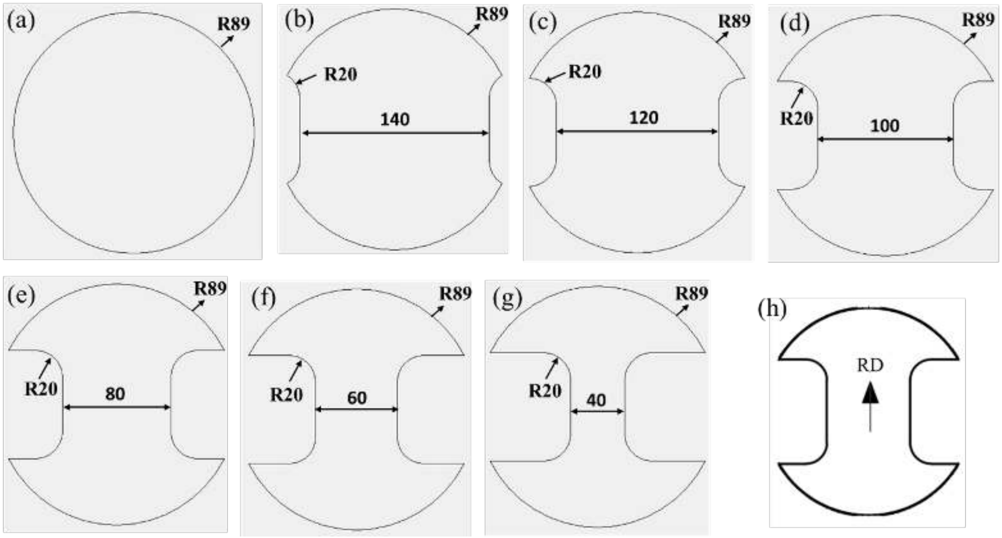

Figure 5: Samples for different loading paths in Nakajima test: (a-g) Specimens geometries for the generation of FLC and (h) preferred orientation of specimens used in FLC testing.

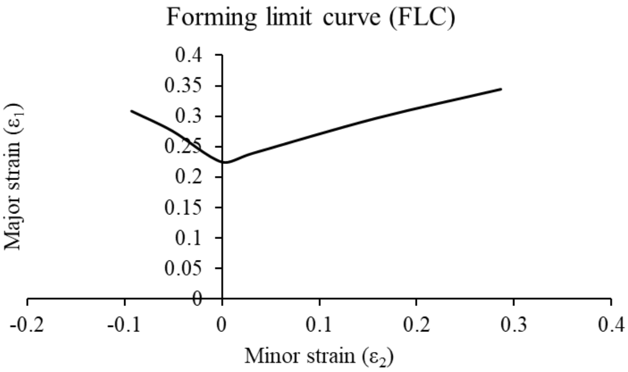

Figure 6: Forming limit curve (FLC) of the base material AA6061

test, and GOM ARAMIS version 6.1 software was used to acquire and process the captured images to calculate strain [51] [52]. The calculated failure strain values were plotted on the forming limit diagram (FLD) to represent the FLC of the material, as shown in Figure 6.

## 5. Results and discussion

Various shapes were formed on the existing setup by RAISF and RAISHF, as shown in Figure 7. Once, different shapes had been formed successfully, several tests were conducted to compare the performance of two processes.

### *5.1. Maximum formable angle and forming limit of RAISF and RAISHF*

In RAISF and RAISHF, the formability limit is decided by the maximum wall angle which can be formed before fracture.To find the maximum formable angle, a variable wall angle conical frustum (VWACF) as suggested by Hussain et al. [4] was fabricated. The generatrix of VWACF is shown in Figure 7 (e). The samples made by RAISF and RAISHF are shown in Figure 7 (f) and Figure 7 (g) respectively. The details of the VWACF obtained by RAISF and RAISHF are given in Table 1.

It can be inferred from Table 1, that improved forming angle and reduced spring back can be achieved by RAISHF compared with RAISF. In case of RAISHF, the forming angle and forming depth increased by 6.67% and 28.47% respectively. As there is a presence of fluid in the back surface of the sheet, this fluid exerts pressure on walls of the cone being formed reducing the stress in the thickness direction ($\sigma_t$) as depicted by equation 5a. This coupled with increase in the tensile meridional stress leads to increase in hydrostatic stress, ensuring the suppression of voids and delay of necking and subsequent failure [53–55]. In addition to this, the improved level of hydrostatic stresses can lead to enhanced ductility due to delay in onset of void growth [29, 56–58] further contributing to enhanced formability.

Once the maximum wall angle was predicted using VWACF test, fixed wall angle conical frustums (FWACF) were successfully fabricated by RAISF(60°) and RAISHF(64°) under the experimental condition, as optimized by straight groove test. The radius of the circular base of the cone was taken as 100 mm. The improved formability was further demonstrated by comparing in-plane strain of FWACF formed by RAISF and RAISHF. To facilitate strain analysis, the undeformed sheets were engraved with a circular grid pattern (diameter = 10 mm), which deformed into an elliptical shape during fabrication. The grid marking process adhered to the method proposed by Keeler [59] and was implemented using a 50 W fiber laser. Various grid patterns and methodologies for grid marking have been

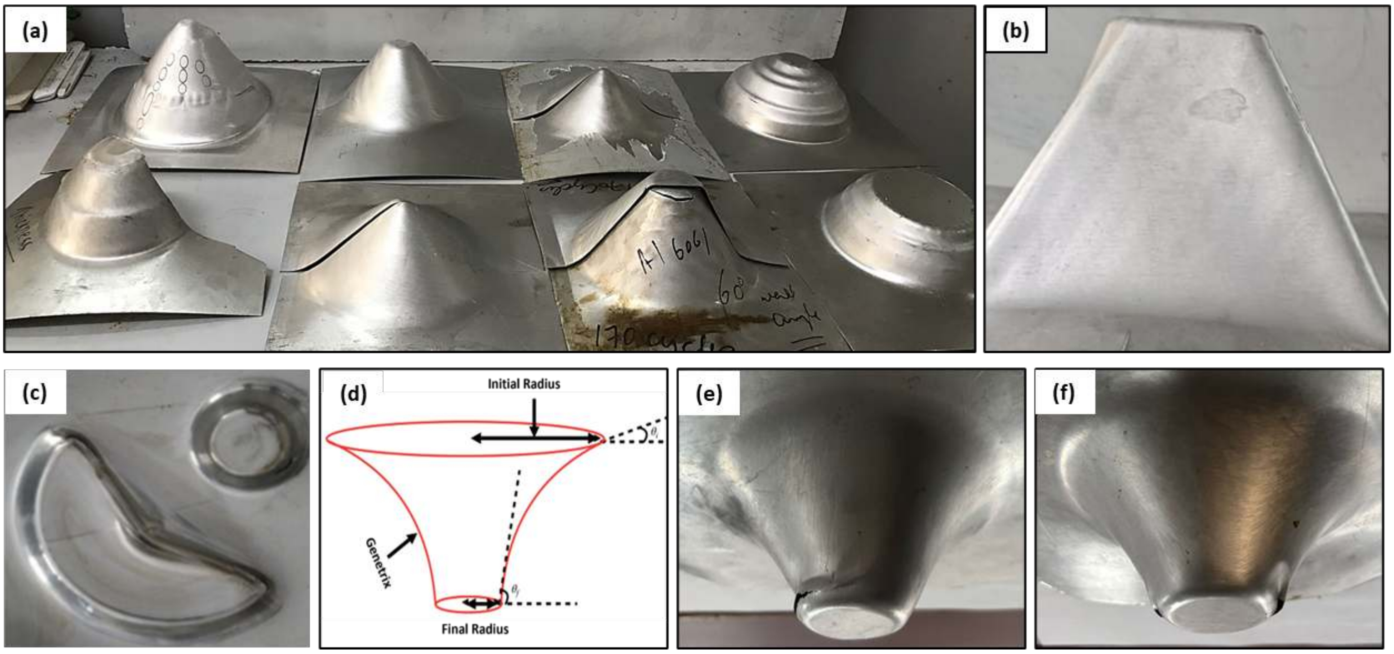

Figure 7: Various shapes fabricated using RAISF and RAISHF: (a) conical and stepped frustums, (b) square pyramid with fixed wall angle (c) multi-feature shape (d) generatrix of VWACF (e),(f) VWACF fabricated by RAISF and RAISHF

detailed in the literature [60]. The major and minor axes of the elliptical grids on the deformed cones were measured using optical microscope, and the true major and minor strains were calculated as.

$$\text{Major strain} = \log\left[\frac{Major\ axis\ length}{Circle\ diameter}\right] \tag{6a}$$

$$\text{Minor} \quad \text{strain} = \log\left[\frac{Minor\ axis\ length}{Circle\ diameter}\right] \tag{6b}$$

The scatter plot of major strain vs. minor strain for RAISF and RAISHF is shown in Figure 8 which represents forming limit for the two processes. It can be seen from Figure 8, that more safe strain can be obtained in RAISHF than in RAISF which further confirms the enhanced formability claim. It can also be seen from equation 5b that tensile stress in meridional direction is increasing which can lead to more stretch along the wall making the circles distort further. It can be stated that fluid underneath the sheet acting as a hydraulic support can give rise to hydrostatic pressure which can contribute to voids suppression, delay in necking and enhanced ductility all of which contribute to greater formability in RAISHF than by RAISF.

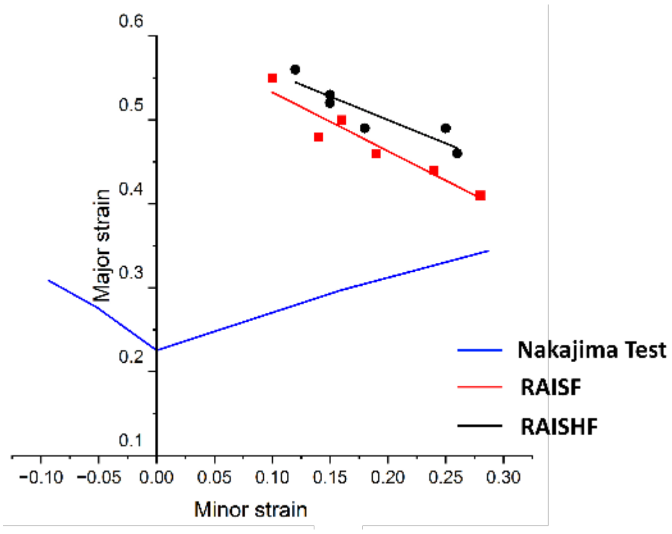

Figure 8: Comparison of forming limit obtained in RAISF and RAISF on Major strain-Minor strain Plot of AA6061

### 5.2. *Thickness distribution and accuracy of formed product*

One of the major advantages of using hydraulic support is improved accuracy of the formed part. For comparing accuracy of the formed product in two processes, FWACF with a similar wall angle of 60° were fabricated using RAISF and RAISHF. These cones, along with samples extracted from them, were further utilized to compare various features and properties of the two processes. To evaluate the thickness distribution and the precision of the formed product, the cone was cut precisely into two halves with wire electro-discharge machining (W-EDM) and the conical region was divided into 7 regions (0-6), as shown in Figure 9(a), region-0 being the undeformed one, where thickness is 1.050 mm. The thickness in different regions was measured by digital micrometer with conical tips and a least count of 0.001 mm. The measurement was repeated four times and average of all four readings has been reported. The thickness plots for the RAISF

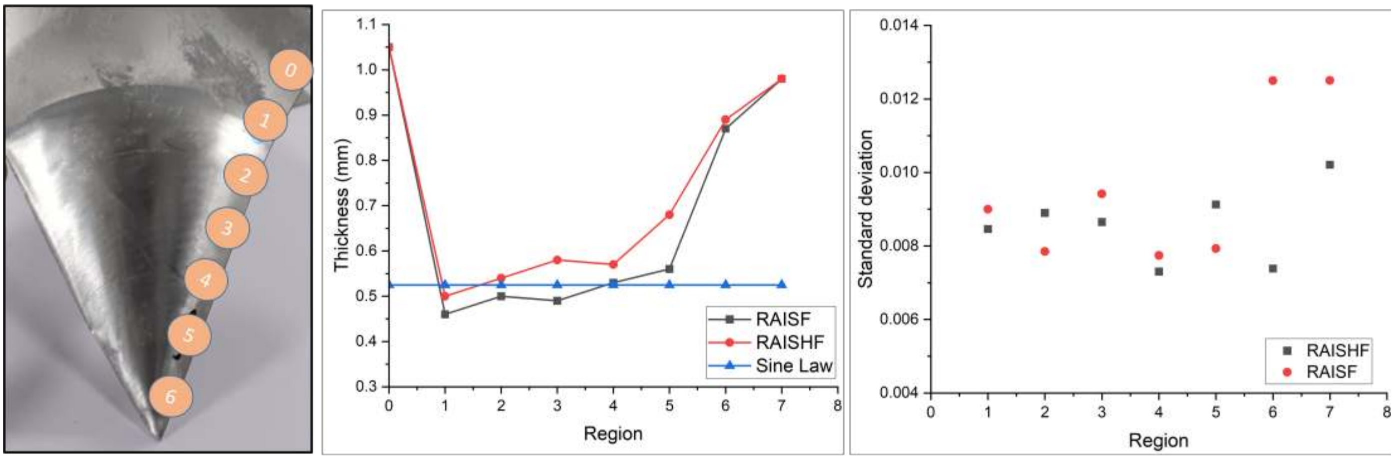

(a) (b) (c)

Figure 9: Comparison of thickness distribution along the length of FWACF: (a) Various regions along the length of the cone where thickness is measured and (b) variation of wall thickness of cones formed by RAISF and RAISHF processes, along the meridional plane. (c) Standard deviation of readings taken

Table 2: Thickness details of sheet along the length of the cone wall

| Process | Average sheet thickness ($t_{avg}$) (mm) | Minimum thickness (mm) |
|---|---|---|
| RAISF | 0.682 ± 0.001 | 0.462 ± 0.001 |
| RAISHF | 0.725 ± 0.001 | 0.503 ± 0.001 |

and RAISHF processes are shown in Figure 9(b). The standard deviation of the readings have been shown in Figure 9 (c). It was found that a certain amount of sheet thinning is associated with both RAISF and RAISHF. The cone was found to be thinnest in the region 1-2 which is region of combined combined bending and stretching. The thickness of the cone was found to be nearly uniform in the regions 2-5. In these regions, the thickness of the sheet can be approximated by sine law. This trend has been frequently reported by previous researchers Ambrogio et al. [61] and Young and Jeswiet [62], who showed that in middle region of the formed cone, thickness prediction by sine law is most accurate. The blue line in Figure 9(b) shows the thickness, as predicted by the sine law for spinning, $t = t_\circ sin(\pi/2 - \theta$ (where $\theta$ is the wall angle and $t_\circ$ is the original sheet thickness) [2]. The average sheet thickness $t_{avg}$ in the regions 1-5, is given in Table 2.

For RAISHF, thickness in the region 1-5 is more than that in RAISF, hence local sheet thinning can be avoided to a significant extent. The average sheet thickness of the cone formed by RAISHF is found to be 6.09% more than that formed by RAISF. As it could be seen in the previous sections that, the thickness stresses get reduced by bringing in the hydraulic pressure, this causes decrease in the thickness strain ($\epsilon_t$). Apparently, the increase in the tensile meridional stress can lead to the larger in plane deformation as found in the elevated FLC of RAISHF. It can be understood that more uniform strain distribution can be observed in RAISHF also reported by FEA analysis by Shang et al. [38, 39]. It has been further observed that the range of deviation of thickness of different regions from average thickness varied from -15.34% to 17.27% in case of RAISF whereas in case of RAISHF the variation lied in the range of -8.84% to 5%. A more uniform thickness distribution can directly make the part more accurate which can be further confirmed by evaluating the extent of spring back.

Spring back is basically deviation of wall angle from theoretical wall angle due to retained elasticity in the sheet after unloading. After the tool leaves the local contact with the sheet, there is an elastic release of deformation due to which spring back occurs. The theoretical wall angle ($\phi_t$) can be simply calculated as ratio of increments in vertical and radial direction as depicted in Figure 10(a) and (b) and can be given as:

$$\phi_t = tan^{-1}(\frac{\Delta Z}{\Delta r}) \tag{7}$$

Due to retained elasticity present in the sheet, actual wall angle ($\phi_a$) is lower than the theoretical wall angle($\phi_t$). The ($\phi_a$) was obtained as:

$$\phi_a = tan^{-1}(\frac{H}{R_u - R_L}) \tag{8}$$

where, H is the vertical height of cone, $R_u$ and $R_L$ are the radius of top and and bottom circle of FWACF respectively. Consequently, spring back was calculated as percentage difference between ($\phi_t$) and ($\phi_a$) given as:

$$\text{Spring back}(\%) = \frac{(\phi_t - \phi_a)}{\phi_t} \times 100 \tag{9}$$

The details of FWACF formed by RAISF and RAISHF formed along with springback observed in both cases have been given in table 3.

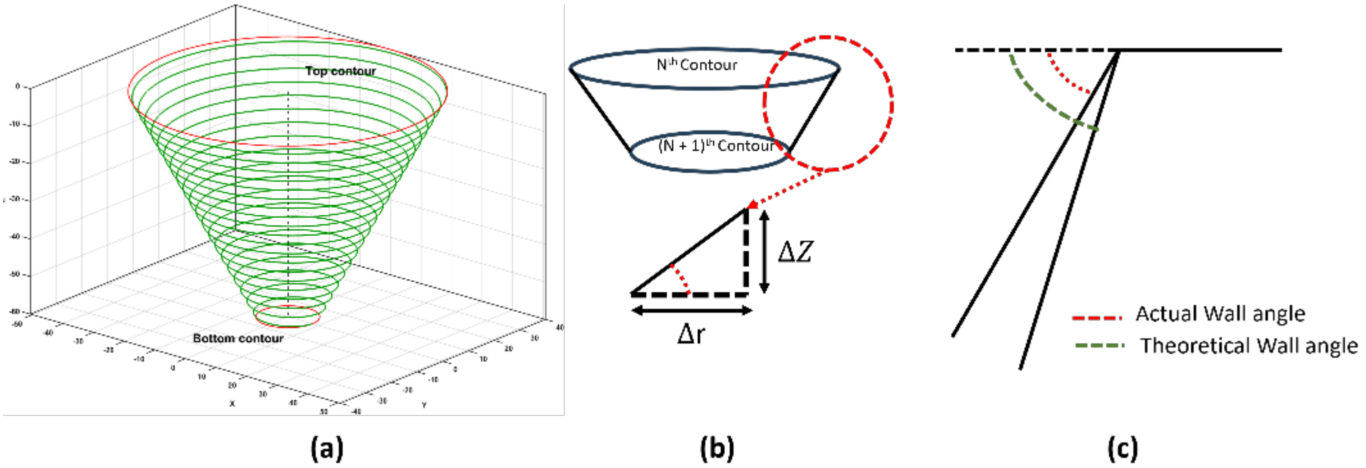

Figure 10: Representation of spring back in ISF: (a) different contours in forming FWACF (b) theoretical wall angle due to increments (c) deviation due to spring back.

Table 3: Details of FWACF with 60° wall angle formed by RAISF and RAISHF

| Process | $\theta_t$ | Cycles ($N$) | $\theta_a$ | Spring back (%) |
|---|---|---|---|---|
| RAISF | 60 | 150 | 53.37 | 11.04 |
| RAISHF | 60 | 150 | 58.21 | 2.97 |

It can be seen from Table 3 that, the spring back in RAISHF reduced significantly in comparison with RAISF. A reduction of 73.09% in spring back was recorded while forming FWACF of 60° wall angle. The presence of the fluid acts as a counter-support during deformation, thereby restricting unwanted material rebound and contributing to the improved dimensional accuracy of the formed part.

### *5.3. Tensile and microhardness test*

To compare tensile properties before and after forming, uniaxial tensile tests have been conducted on the samples, on a 100 kN INSTRON (MODEL 8801). The samples have been prepared as per the standard ASTM/E8 [63]. Since there can be anisotropy in the formed product due to forming direction, hence the test samples have been prepared in three orientations: namely, (a) along the length of the formed cone (meridional direction) (b) along the direction of the tool motion (circumferential direction) (c) along 45° direction to meridional direction as shown in Figures 11(a), (b) and (c) respectively.

The engineering stress-strain curves for the various tests conducted on the meridional, circumferential, and 45° direction samples are shown in Figure 11 (e), (f) and (g) respectively and corresponding tensile properties obtained in various directions are presented in Table 4. It is worthwhile to note that tensile test performed on samples taken from FWACFs has pre-strain leading to reduced elongation with respect to heat treated samples. It can be seen from Table 4, that tensile properties in different directions were different, showing anisotropy due to tool direction and induced strain hardening. The strength of samples taken from the cone formed by RAISHF was found to be relatively less. However, elongation was more in those samples. The relatively lower strength observed in hydroformed samples can be attributed to stress delocalization induced by the static fluid pressure providing hydraulic support from the backside. In RAISF, localized strain accumulation promotes work hardening, whereas RAISHF ensures a more uniform stress distribution due to the continuous support of the fluid pressure preventing severe plastic deformation in localized regions, thereby limiting the formation of high-dislocation density zones that typically contribute to strengthening. Additionally, more homogeneous strain distribution results in reduced work hardening effects, as the material undergoes gradual deformation rather than experiencing abrupt strain localization.

The microhardness values of the samples taken from different regions of FWACFs were measured to further strengthen above claim. Testing was carried out on OMNITECH microhardness testing machine. The applied load was 100 g and indentation time was 10 seconds. For each sample, 4 micro measurements were taken at different points and average of the four values has been taken as microhardness of that region. Average microhardness of undeformed AA6061 sheet is found to be VHN 64. The respective values of microhardness recorded in different region of FWACF formed by the RAISF and RAISHF are given in Table 5.

As shown in Table 5, the microhardness of the deformed samples is higher than that of the heat-treated ones, which is expected due to strain hardening. However, the samples from FWACF formed by RAISHF exhibit lower microhardness compared to those formed by RAISF. This can be explained by the nature of hydroforming,

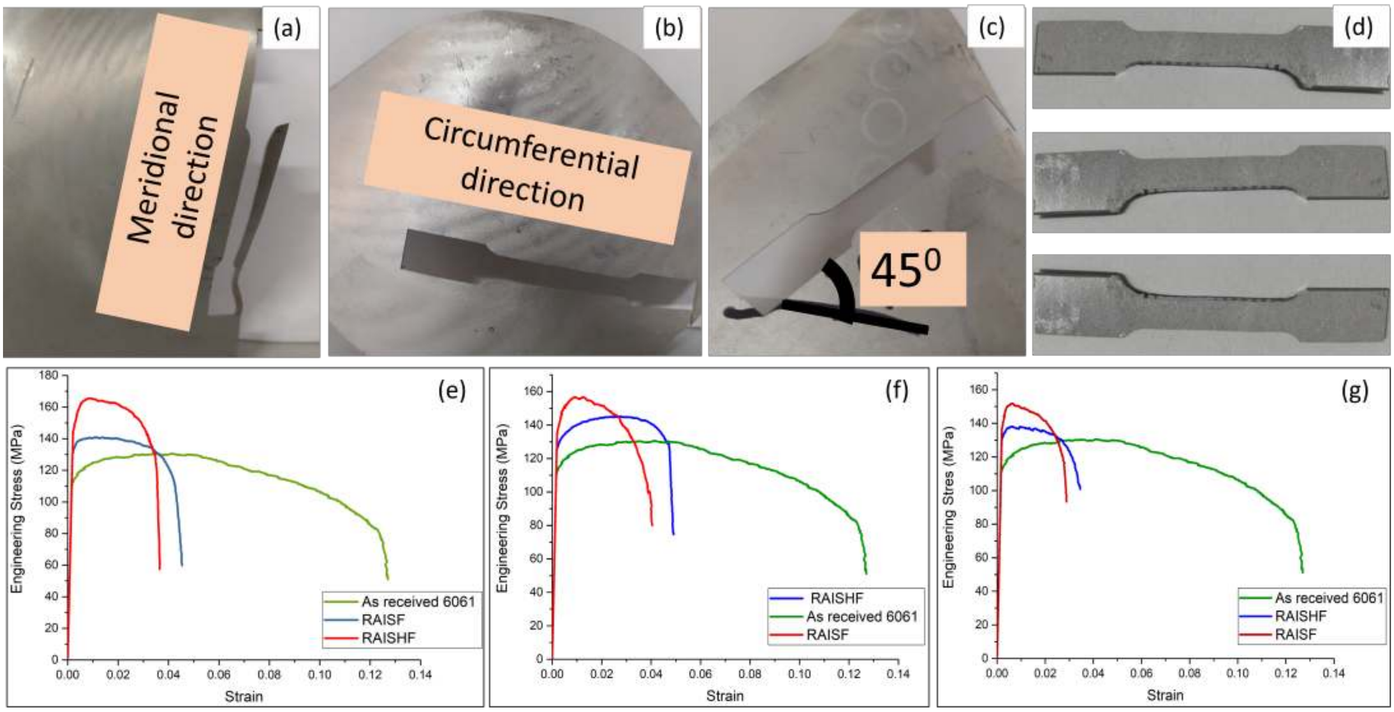

Figure 11: Tensile samples and corresponding stress-strain response:(a)-(c)Tensile samples made in different orientations of the cone (d) various tensile samples. (e)-(f) Stress -strain plot along: (e) circumferential direction, (e) meridional direction, and (f) at 45° from the meridional direction.

Table 4: Tensile properties of the cones formed by RAISF and RAISHF, in different orientations.

| | Tensile properties along circumferential direction | | |
|---|---|---|---|
| Parameters | Heat treated | RAISF | RAISHF |
| 0.2% offset YS (MPa) | 112 | 142 | 133 |
| UTS (MPa) | 127 | 162 | 136 |
| Elongation (%) | 12.16 | 3.81 | 4.14 |
| | Tensile properties along meridional direction | | |
| 0.2% offset YS(MPa) | 112 | 130 | 123 |
| UTS (MPa) | 127 | 157 | 141 |
| Elongation (%) | 12.16 | 4.12 | 5.04 |
| | Tensile properties of the cone along 45 degrees | | |
| 0.2% offset YS(MPa) | 112 | 145 | 126 |
| UTS (MPa) | 127 | 146 | 128 |
| Elongation (%) | 12.16 | 2.54 | 4.08 |

| Region | RAISF (VHN) | RAISHF (VHN) |
|---|---|---|
| 0 | 75.0 | 75 |
| 1 | 81.6 | 74.8 |
| 2 | 90.5 | 70.5 |
| 3 | 90.2 | 81.2 |
| 4 | 104.2 | 80.2 |
| 5 | 93.5 | 98.2 |
| 6 | 83.2 | 76.0 |

Table 5: Average microhardness values obtained in different regions of the formed cones.

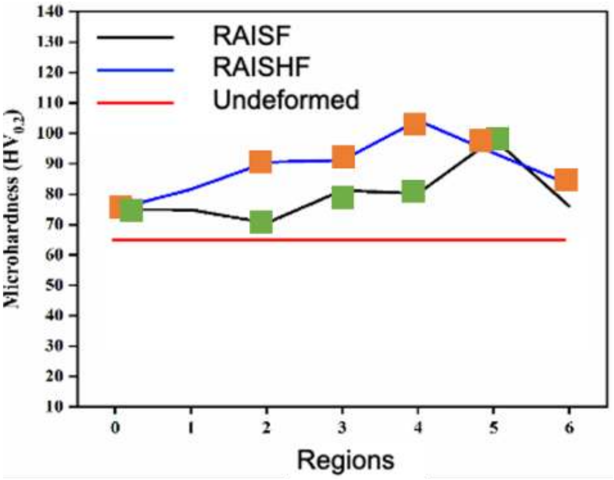

Figure 12: Comparison of microhardness of the cones formed by RAISF and RAISHF

where the uniform fluid pressure reduces localized plastic deformation, leading to a lower dislocation density and less work hardening. On the other hand, RAISF, which lacks hydraulic support, results in higher localized strain, causing more work hardening and, consequently, higher microhardness.

Figure 12 further illustrates that microhardness is highest in the middle region of the cone, suggesting that this area has undergone the most strain hardening due to deformation. Although hydraulic pressure in RAISHF enhances formability by reducing localized plastic deformation, it also results in lower dislocation pile-up, leading to reduced hardness and strength due to strength-ductility trade-off [64], where uniform deformation minimizes strain hardening. However, post-forming heat treatments can restore the strength while retaining the improved formability.

### 5.4. *Residual Stress*

It has been established that the hydraulic pressure in RAISHF helps in delocalizing strain leading to more uniform strain distribution throughout the formed part. This strain delocalization is expected to influence the residual stress state, which affects the mechanical behavior and fatigue performance of the formed components [65, 66]. The residual stress on the free surface of the samples taken from region 4 of the cone was measured using high resolution XRD. '$d - sin^2\Psi$' methodology was adopted for calculation of residual stresses in the samples [67–69]. Three samples were taken; (a) undeformed sample (b) sample from FWACF made by RAISF (c) sample from FWACF made by RAISHF. The definition of specimen frame of reference (FOR), rotated user FOR and different rotation and tilt angles are shown in Figure 13. $S_i$ represents the specimen FOR where $S_3$ is perpendicular to specimen plane and $S_1$ and $S_2$ represent two perpendicular directions in the plane of the specimen. $L_i$ is the user FOR with $L_3$ perpendicular to the (hkl) plane undergoing diffraction and $L_1$ and $L_2$ represent two perpendicular directions in (hkl) plane. Strain was calculated by shift in the diffraction peak which gives the change in inter planar spacing. The strain component $\epsilon_{\phi\psi}$ can be written for the rotation angle ($\phi$) and tilt angle ($\psi$) with inter planar spacing determined from the diffraction peak for a certain plane as given by:

$$\epsilon_{\phi\psi} = \frac{d_{\phi\psi} - d_0}{d_0} \tag{10}$$

where $d_{\phi\psi}$ is the inter planar spacing at $(\phi, \psi)$ and $d_0$ is the inter planar spacing for strain free lattice spacing. The plot between $d_{\phi\psi}$ and $sin^2\psi$ was made by linear fit and measuring the slope and intercept yielded the value of stress components. If there is presence of shear components then $\psi$ − splitting occurs. The nature of residual stress on the surface of both the samples, taken from FWACFS fabricated by RAISF and RAISHF was found to be tensile. Similar results for ISF was obtained using FEA by Kumar et al. [68] Additionally, because of $\psi$ − split, it can be said that shear stress is also produced during both of the processes. The values of stresses for the undeformed, RAISF and RAISHF samples for $\phi = 0°$, 45° and 90° are given in Table 6.

It can be seen from Table 6 that, the nature of residual stress was tensile on the surface of the formed cone by both the processes, and was relatively larger in the cone formed by RAISF across all orientations. This is because RAISF causes more localized straining and work hardening, leading to higher stress levels. In contrast, RAISHF uses hydraulic pressure to distribute strain more evenly, reducing stress buildup and creating a more uniform stress distribution.

### 5.5. *Microstructure evolution by EBSD and SEM*

The study of microstructure and texture evolution was done by performing Electron Back Scattered Diffraction (EBSD) on Zeiss Gemini, equipped by OXFORD fast CCD detector. For analysis of data obtained from EBSD, the TSL-OIM software was used. The EBSD scans were taken

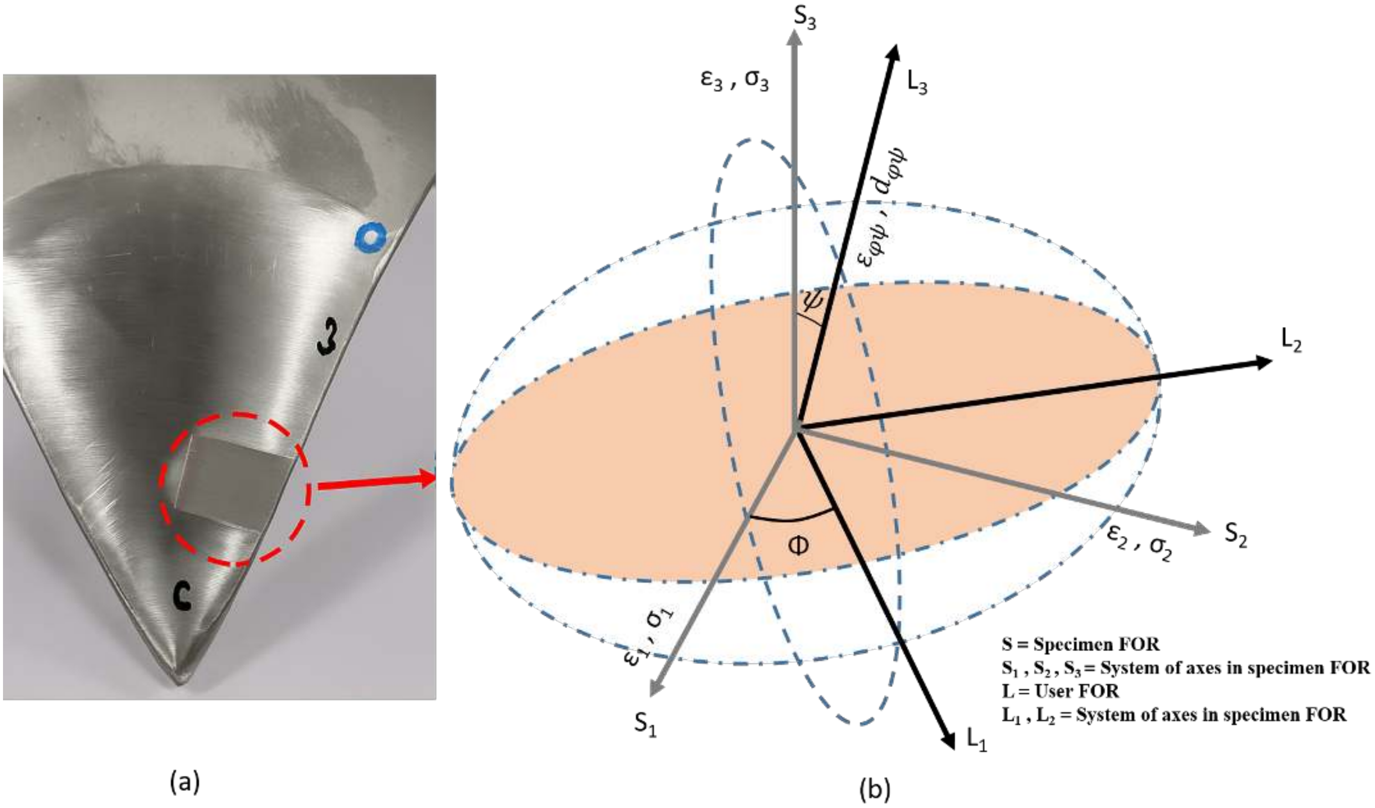

Figure 13: Residual stress study: (a) Sample for XRD and (b) definition of different FORs and different angles for XRD examination.

| Sample | $\phi = 0°$ | $\phi = 45°$ | $\phi = 90°$ |
|---|---|---|---|
| Undeformed | $8.4 \pm 0.3$MPa | $43.8 \pm 0.3$MPa | $78.8 \pm 0.3$MPa |
| RAISF | $52.3 \pm 1.1$MPa | $64.9 \pm 1.1$MPa | $77.5 \pm 1.1$MPa |
| RAISHF | $45.9 \pm 0.4$MPa | $44.5 \pm 0.4$MPa | $43.0 \pm 0.4$MPa |

Table 6: Values of residual stresses in different samples, at different orientations

with a step size of 0.15 $\mu$m. Three samples were tested: (a) undeformed sample (UD) (b) sample taken from region 4 of FWACF formed by RAISF (c) sample taken from region 4 of FWACF formed by RAISHF. EBSD data was used for getting inverse pole Figure (IPF), image quality (IQ) maps, and grain average misorientation (GAM) plot. The IPF plot, IQ map and GAM plot of undeformed samples are given in Figure 14. It may be observed from Figure 14 (a) and (b), that equiaxed fully recrystallized grains were present as the sheet was in fully annealed condition. The average grain size was found to be 8.3 $\mu$m. The grains appeared to be relaxed due to absence of any strain as annealing caused recrystallization giving rise to stress free grains. Figure 15 gives the plot of number fraction vs. misorientation angle. The misorientation angle greater and less than 15°, are associated with high angle grain boundary (HAGB), and low angle grain boundary (LAGB) respectively. The misorientation angle analysis data shown in Figure 15 (a) shows that high density of high angle grain boundaries (HAGBs) was present in the undeformed sample. It has been further calculated that 26.2% of grains were separated by low angle boundaries and 73.8% of the grains were separated by high angle boundaries. As FWACF was formed, the sheet gets deformed, due to which, the grains got elongated along the tool motion. The IPF of sample deformed by RAISF and RAISHF are shown in Figure 16(a) and (d) respectively.

It was observed that grains became refined due to cold work imparted to the sheet. The average size of grains in the samples obtained from the FWACFs formed by RAISF and RAISHF, were found to be 3.63 $\mu$m and 4.51 $\mu$m respectively. Refined grains can be seen from the IPFs with different colors for LAGBs and HAGBs shown in Figure 16 (a) and (d). Because high plastic deformation occurred in both the processes, it caused grain fragmentation leading to fine grain evolution. It can be seen from IQ map of

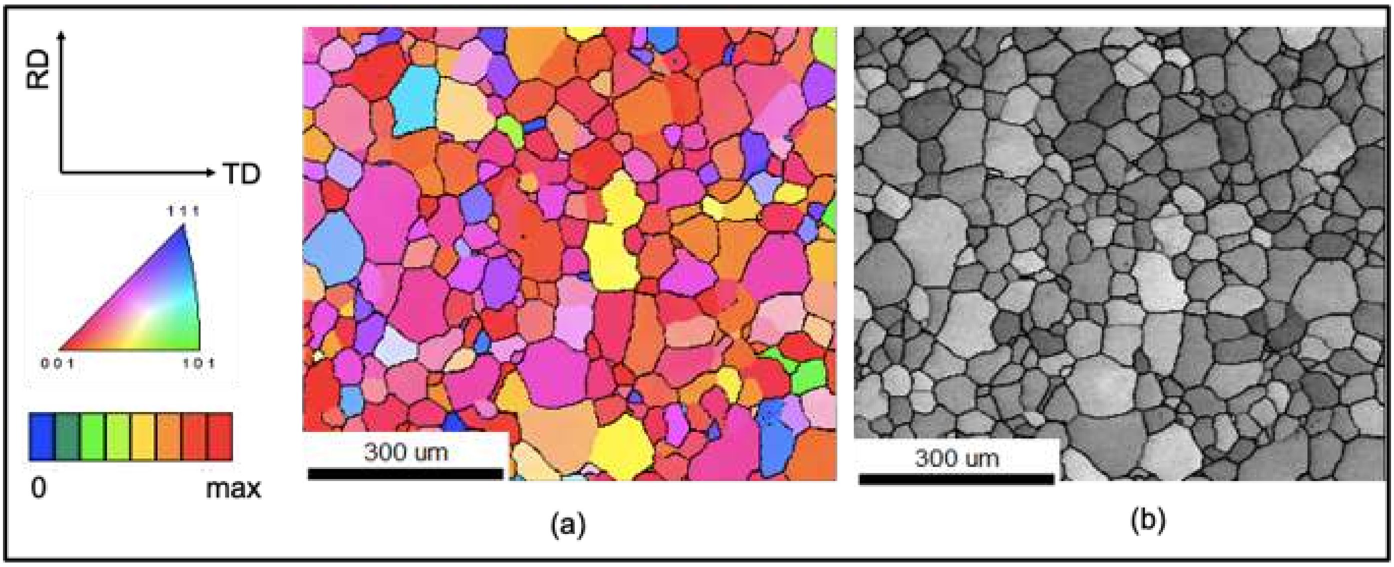

Figure 14: EBSD of undeformed AA6061 in annealed condition: (a) IPF plot and (b) IQ map

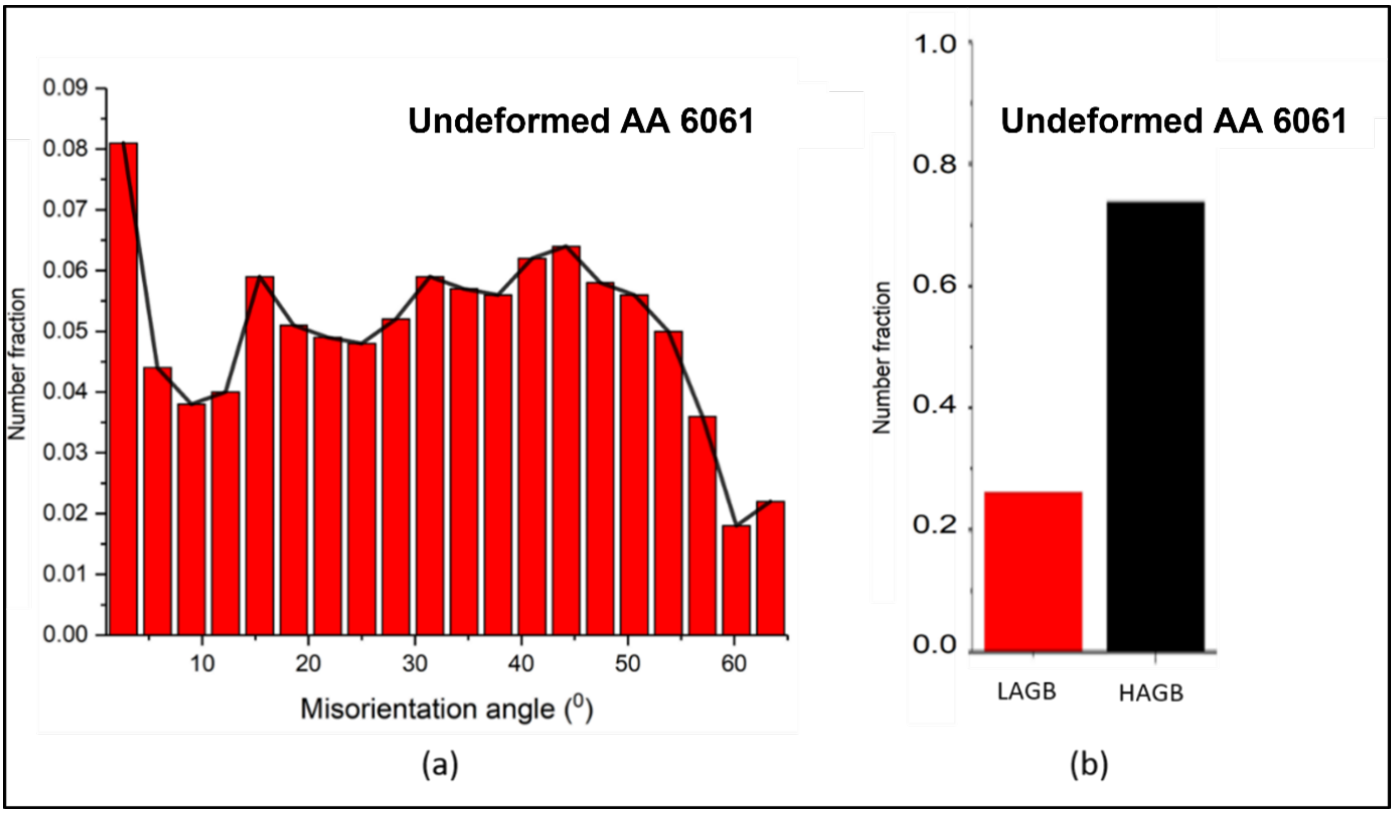

Figure 15: Distribution of misorientation angle in the undeformed AA6061 sample: (a) number fraction vs misorientation angle plot (b) distribution of grain boundaries in LAGBs and HAGBs

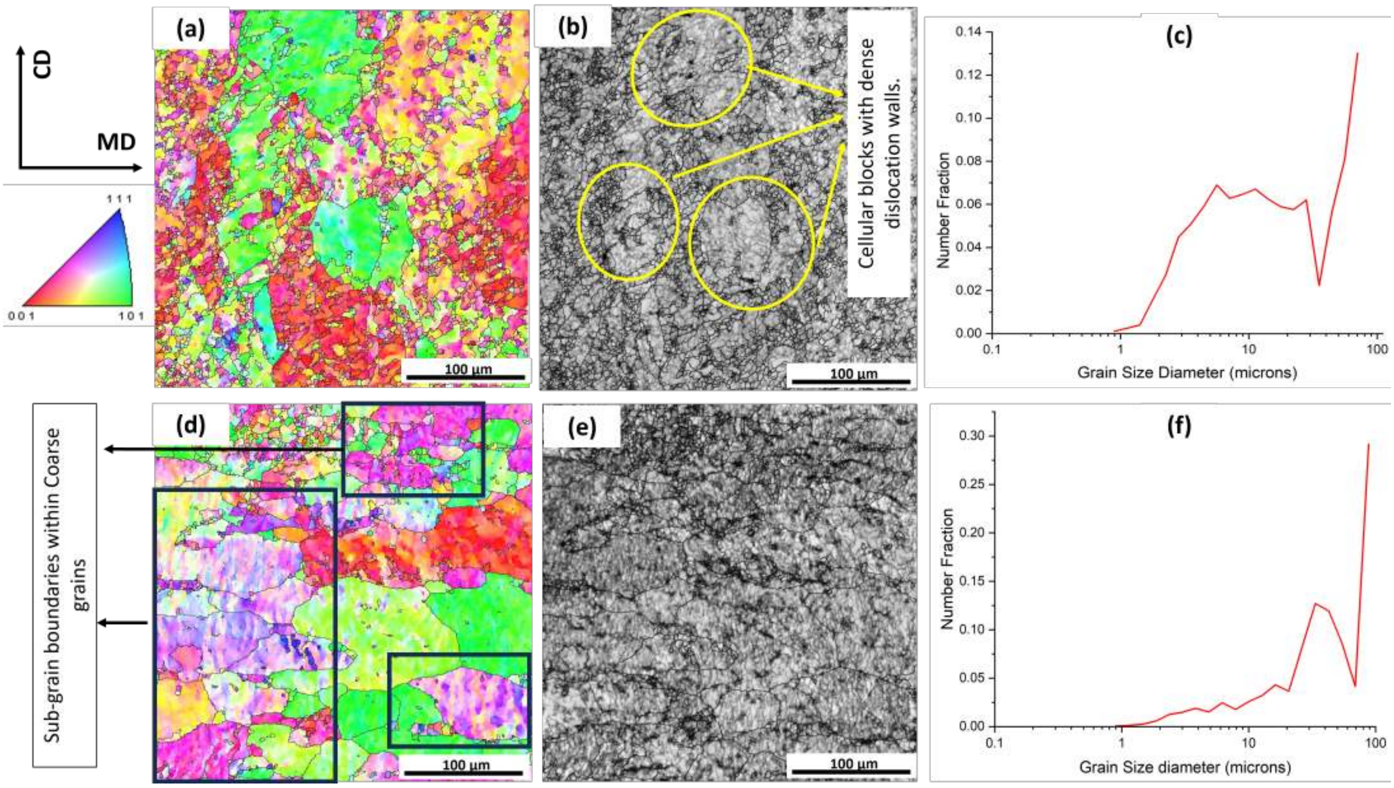

Figure 16: IPF and IQ maps of deformed samples: (a) IPF of sample formed by RAISF, (b) IQ map of sample formed by RAISF, (c) Grain size distribution in sample formed by RAISF(d) IPF of sample formed by RAISHF, and (e) IQ map of sample formed by RAISHF (f)Grain size distribution in sample formed by RAISF

RAISF sample, that there are cell blocks present with dense dislocation walls. The cell blocks form at the start of the deformation which activates different slip systems in a grain [70, 71]. It was observed from IPF of the undeformed sample that there were LAGBs present in it. As the sheet gets deformed, these LAGBs act as a site for nucleation of new grains and the formed cellular blocks were surrounded by dense dislocation walls. In case of RAISHF, it was observed that apart from cell blocks with dense dislocation walls, coarse grains were present which contained fine sub grain boundaries which can be observed by color gradient within the coarse grains in Figure 16 (d). The grain size distribution of the grains present in sample formed by RAISF and RAISHF can be seen from 16 (c) and (f).

Although, in case of both RAISF and RAISHF grain refinement occurred but in case of RAISF finer grains were present. Presence of finer grains in RAISF sample can also be confirmed by the results of tensile test and Hall-Petch according to which, sample with finer grains have higher strength. It has been observed from the tensile test that the strength of the RAISF sample is more than that of the RAISHF sample. A similar result for incremental sheet forming was observed by Chang et al. [71] and Kumar et al. [72][63] where finer grains were observed in the deformed sample. In case of RAISHF more strain was obtained, and the result is supported by Kernel misorientation map (KAM). The KAM plot of RAISF and RAISHF samples are shown in Figure 17(b) and (e) respectively. It can be seen from KAM plot that RAISHF sample underwent more strain during the process. Further, it can be observed from Figure 17(a) and (c) that high density of low angle or sub-grain boundaries were present in both the samples. LAGBs are a characteristic of the processes involving cold work [73–75]. Further, in case of RAISF, majority of LAGBs lied in the region of 5°–15° whereas in case of RAISHF they are found to be in the region of 1°–5°. During the RAISF process since the material experienced more thinning, it underwent more through thickness deformation , leading to more dislocations and resulting in dynamic recrystallization of fine grains. Whereas in the case of the RAISHF process, since the samples were thicker than that of the RAISF process, the process of dynamic recrystallization was incomplete. It can be seen from the IPF of RAISHF sample in Figure 16(d) that there are more sub grain boundaries and higher KAM also reflect higher dislocations in the samples.

## 6. Conclusion

In the current work, a comparative study of forming of the AA6061 sheet by two forming processes, RAISF and RAISHF, has been presented. Tensile test and Erichsen ductility test have been performed to evaluate tensile

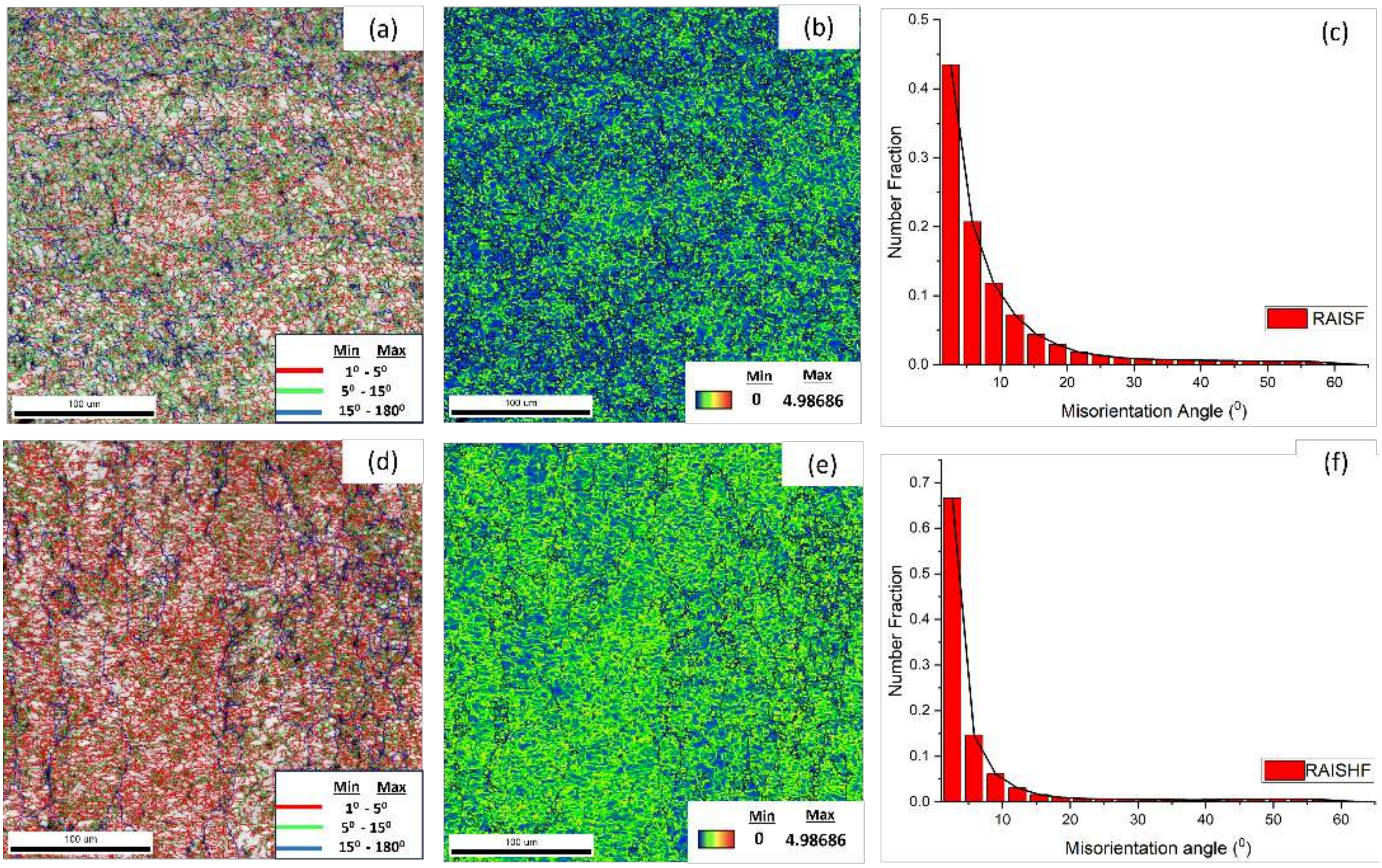

Figure 17: Grain boundary and KAM plots of deformed samples: (a) Grain boundary map of RAISF sample, (b) KAM map of RAISF sample, (c) distribution of misorientation angle in the RAISF sample, (d) grain boundary map of RAISHF sample, (e) KAM map of RAISHF sample, and (f) distribution of misorientation angle in the RAISHF sample.

properties and formability of the sheet before deformation. Several shapes have been made using the two processes and their properties have been compared. Experiments have been performed on parameters obtained from straight groove test and the following conclusions are drawn.

- The role of fluid pressure in RAISHF was studied using a through thickness element and was found that fluid pressure plays a vital role in delocalization of thickness stress leading to uniform strain distribution and improved formability

- More forming depth and lesser spring back was found in the cones fabricated by RAISHF than by RAISF.

- It was found from grid analysis that more in-plane strain can be obtained in RAISHF than in RAISF. Hence forming limit is elevated by using hydraulic support in RAISF

- Due to hydrostatic nature of fluid pressure from back, more uniform thickness distribution was observed in case of RAISHF than that of RAISF.

- The micro hardness of the samples was measured and was found that the sample in the middle region of FWACF was hardest for both RAISF and RAISHF. However, microhardness in case of RAISF is found to be higher than that in RAISHF.

- EBSD analysis has been carried out for studying the microstructural evolution in the undeformed sheet and formed by RAISF & RAISHF. It has been observed that significant grain refinement occurred from RAISF and RAISHF. Finer grains were found to be present in case of RAISF than in RAISHF.

## Acknowledgements

The authors are grateful to DST-SERB for sponsoring the work through project MMER/2014/0068 titled ‘Design, Development and Fabrication of an Incremental sheet hydroforming machine setup’. EJB is grateful for the UKRI Future Leaders’ Fellowship funding (MR/V02261X/1) supporting this work. For the purpose of open access, the authors have applied a Creative Commons Attribution (CC BY) license to any Author Accepted Manuscript version arising from this submission.

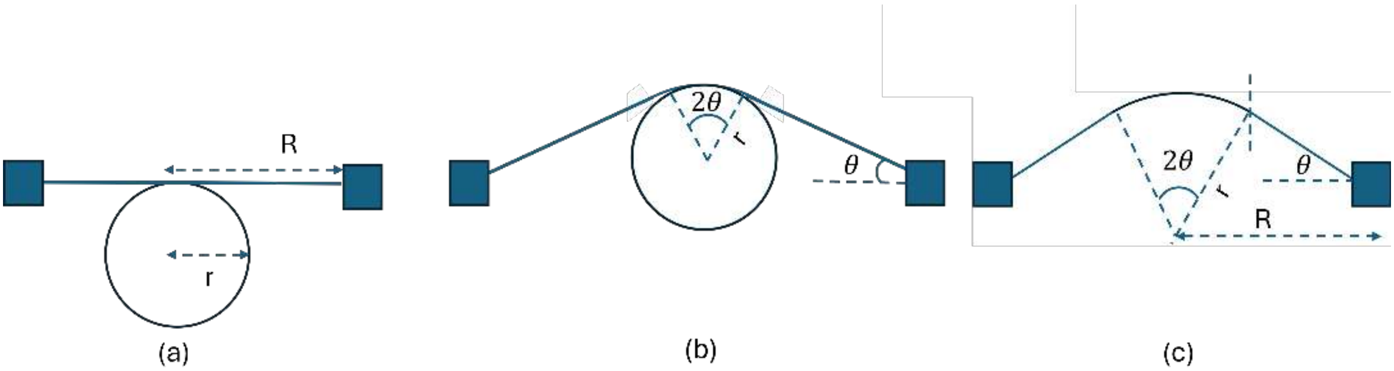

Figure A.1: Strain rate calculation in Nakajima test : (a) tool - sheet geometry before deformation (b) Indentation post deformation (c) detailed indentation geometry

## Data Availability statement

The raw/processed data required to reproduce these findings cannot be shared at this time as the data also forms part of an ongoing study.

## Consent for publication

Consent for publication was obtained from all participants.

## Conflict of interest

The authors declare that they have no conflict of interest.

## Appendix A. Strain rate calculation in Nakajima Test

As can be seen from the given figure A.1 that, as tool(of tool radius 'r') indents to form the dome of height 'h' on the Nakajima sample of radius R, with a tool speed (V).

The strain ($\epsilon$) obtained as a a result of deformation can be is given as

$$\epsilon = \frac{1}{R} \cdot \left[ \frac{r\,\theta + (R - r\sin\theta) - R}{R} \right] \tag{A.1}$$

The strain rate can be determined by differentiating equation A.1

$$\dot{\epsilon} = \frac{1}{R} \left[ r\ + R\,\sec\theta\,\tan\theta - r\,\tan^2\theta \right] \dot{\theta} \tag{A.2}$$

the dome height ($h$) can be determined as

$$h = (r - r\cos\theta) + (R - r\sin\theta)\tan\theta \tag{A.3a}$$

$$h = r - r\sec\theta + R\tan\theta \tag{A.3b}$$

On differentiating A.3b, and writing it as tool speed the equation can be converged as

$$\dot{h} = V = (-r\,\sec\theta\,\tan\theta + R\,\tan^2\theta)\dot{\theta} \tag{A.4}$$

The strain rate can be evaluated by dividing equation A.2 by equation A.4 as

$$\frac{\dot{\epsilon}}{\dot{h}} = \frac{1}{R} \cdot \frac{\left[ r\ + R\,\sec\theta\,\tan\theta - r\,\tan^2\theta \right] \dot{\theta}}{(-r\,\sec\theta\,\tan\theta + R\,\tan^2\theta)\dot{\theta}} \tag{A.5}$$

Equation A.5 can be finally simplified to get the strain rate as

$$\dot{\epsilon} = \frac{V\mathrm{sin}\theta}{R} \tag{A.6}$$

As $\theta$ varies during the course of deformation, the average strain rate over the 0 to $\theta$ can be written as

$$\text{Average strain rate} = \frac{V}{R} \cdot \frac{\int_0^\theta \sin\theta\, d\theta}{\int_0^\theta d\theta} = \frac{V}{R}\left(\frac{1-\cos\theta}{\theta}\right) \tag{A.7}$$

As the sample size R varies for different loading paths, the corresponding dome heights (h) was measured and $\theta$ was evaluated which was used for calculation of average strain rate as given in table A.1.

| **R** | **h** | $\theta$ (°) | $\theta$ **(rad)** | **Avg Strain Rate** |
|---|---|---|---|---|
| 89 | 25.96 | 19.98 | 0.3485 | 0.0019 |
| 70 | 24.05 | 28.17 | 0.4914 | 0.0034 |
| 60 | 22.41 | 37.71 | 0.6578 | 0.0053 |
| 50 | 18.09 | 31.40 | 0.5477 | 0.0053 |
| 40 | 17.01 | 25.73 | 0.4488 | 0.0055 |
| 30 | 20.84 | 20.75 | 0.3619 | 0.0060 |
| 20 | 23.27 | 14.60 | 0.2546 | 0.0063 |

Table A.1: Strain rate data for varying R and h

## References

[1] W. Emmens, G. Sebastiani, A. H. van den Boogaard, The technology of incremental sheet forming—a brief review of the

history, Journal of Materials processing technology 210 (2010) 981–997.

[2] T. Kim, D.-Y. Yang, Improvement of formability for the incremental sheet metal forming process, International Journal of Mechanical Sciences 42 (2000) 1271–1286.

[3] W. Emmens, A. H. van den Boogaard, An overview of stabilizing deformation mechanisms in incremental sheet forming, Journal of Materials Processing Technology 209 (2009) 3688–3695.

[4] G. Hussain, N. Hayat, G. Lin, Pyramid as test geometry to evaluate formability in incremental forming: Recent results, Journal of mechanical science and technology 26 (2012) 2337–2345.

[5] S. Bharti, E. Paul, A. Uthaman, H. Krishnaswamy, A. Klimchik, R. Abraham Boby, Systematic analysis of geometric inaccuracy and its contributing factors in roboforming, Scientific Reports 14 (2024) 20291.

[6] S. Mohanty, S. P. Regalla, Y. Daseswara Rao, Robot-assisted incremental sheet metal forming under the different forming condition, Journal of the Brazilian Society of Mechanical Sciences and Engineering 41 (2019) 1–12.

[7] G. Fan, L. Gao, G. Hussain, Z. Wu, Electric hot incremental forming: A novel technique, International Journal of Machine Tools and Manufacture 48 (2008) 1688–1692.

[8] A. Al-Obaidi, V. Kräusel, D. Landgrebe, Hot single-point incremental forming assisted by induction heating, The International Journal of Advanced Manufacturing Technology 82 (2016) 1163–1171.

[9] S. A. Singh, S. Priyadarshi, P. Tandon, Comparative study of incremental forming and elevated temperature incremental forming through experimental investigations on aa 1050 sheet, Journal of Manufacturing Science and Engineering 143 (2021) 064501.

[10] J. Duflou, B. Callebaut, J. Verbert, H. De Baerdemaeker, Laser assisted incremental forming: formability and accuracy improvement, CIRP annals 56 (2007) 273–276.

[11] A. Göttmann, J. Diettrich, G. Bergweiler, M. Bambach, G. Hirt, P. Loosen, R. Poprawe, Laser-assisted asymmetric incremental sheet forming of titanium sheet metal parts, Production Engineering 5 (2011) 263–271.

[12] S. Amini, A. Hosseinpour Gollo, H. Paktinat, An investigation of conventional and ultrasonic-assisted incremental forming of annealed AA1050 sheet, The International Journal of Advanced Manufacturing Technology 90 (2017) 1569–1578.

[13] Y. Li, X. Chen, J. Sun, J. Li, G. Zhao, Effects of ultrasonic vibration on deformation mechanism of incremental point-forming process, Procedia Engineering 207 (2017) 777–782.

[14] H. Meier, B. Buff, V. Smukala, Robot-based incremental sheet metal forming–increasing the part accuracy in an automated, industrial forming cell, Key Engineering Materials 410 (2009) 159–166.

[15] B. Ilangovan, Fixtureless automated incremental sheet metal forming, Ph.D. thesis, Loughborough University, 2016.

[16] G. Hirt, R. Kordtomeikel, T. Bremen, M. Laugwitz, D. Bailly, On the geometrical accuracy in incremental sheet forming, in: Forming the Future: Proceedings of the 13th International Conference on the Technology of Plasticity, Springer, 2021, pp. 507–521.

[17] H. Ren, J. Xie, S. Liao, D. Leem, K. Ehmann, J. Cao, In-situ springback compensation in incremental sheet forming, CIRP Annals 68 (2019) 317–320.

[18] A. Qadeer, G. Hussain, M. Alkahtani, J. Buhl, Springback behavior of a metal/polymer laminate in incremental sheet forming: stress/strain relaxation perspective, Journal of Materials Research and Technology 23 (2023) 1725–1737.

[19] H. Lu, M. Kearney, C. Wang, S. Liu, P. A. Meehan, Part accuracy improvement in two point incremental forming with a partial die using a model predictive control algorithm, Precision Engineering 49 (2017) 179–188.

[20] Y. Kumar, S. Kumar, Experimental and analytical evaluation of incremental sheet hydro-forming strategies to produce high forming angle sheets, Heliyon 5 (2019).

[21] C. Hartl, Research and advances in fundamentals and industrial applications of hydroforming, Journal of Materials Processing Technology 167 (2005) 383–392.

[22] L. Lang, Z. Wang, D. Kang, S. Yuan, S.-H. Zhang, J. Danckert, K. B. Nielsen, Hydroforming highlights: sheet hydroforming and tube hydroforming, Journal of materials processing technology 151 (2004) 165–177.

[23] S. Zhang, Z. Wang, Y. Xu, Z. Wang, L. Zhou, Recent developments in sheet hydroforming technology, Journal of Materials Processing Technology 151 (2004) 237–241.

[24] S. Chinchanikar, H. Mulik, P. Varude, S. Atole, N. Mundada, A review of emerging hydroforming technologies: design considerations, parametric studies, and recent innovations, Journal of Engineering and Applied Science 71 (2024) 205.

[25] L. Lang, J. Danckert, K. B. Nielsen, Investigation into hydrodynamic deep drawing assisted by radial pressure: Part i. experimental observations of the forming process of aluminum alloy, Journal of Materials Processing Technology 148 (2004) 119–131.

[26] D. Kong, L. Lang, Z. Sun, S. Ruan, S. Gu, A technology to improve the formability of thin-walled aluminum alloy corrugated sheet components using hydroforming, The International Journal of Advanced Manufacturing Technology 84 (2016) 737–748.

[27] Z. Sun, L. Lang, Effect of stress distribution on springback in hydroforming process, The International Journal of Advanced Manufacturing Technology 93 (2017) 2773–2782.

[28] H. L. D. Pugh, The mechanical properties and deformation characteristics of metals and alloys under pressure, ASTM International, 1965.

[29] B. Avitzur, B. Avitzur, Pressure-induced ductility, J. Eng. Ind. 92 (1970) 419–426. doi:`10.1115/1.3427764`.

[30] A. J. Martínez-Donaire, M. Borrego, D. Morales-Palma, G. Centeno, C. Vallellano, Analysis of the influence of stress triaxiality on formability of hole-flanging by single-stage spif, International Journal of Mechanical Sciences 151 (2019) 76–84.

[31] K. McLoughlin, A. Cognot, E. Quigley, Dieless manufacturing of sheet metal components with non rigid support, Proc. SheMet 2003 (2003) 123–130.

[32] J.-H. Yu, K.-S. Jung, M. Murugesan, W.-J. Chung, C.-W. Lee, Study on the incremental sheet metal forming process using a metal foam as a die, International Journal of Material Forming 15 (2022) 71.

[33] H. Ichihara, A. Sekiguchi, Development of elastomer-based incremental sheet forming method for curved products, Procedia Manufacturing 15 (2018) 1184–1191.

[34] S. Zhang, G. Tang, Z. Li, X. Jiang, K. Li, Experimental investigation on the springback of AZ31B mg alloys in warm incremental sheet forming assisted with oil bath heating, The International Journal of Advanced Manufacturing Technology 109 (2020) 535–551.

[35] N. B. Khalifa, S. Thiery, Incremental sheet forming with active medium, CIRP Annals 68 (2019) 313–316.

[36] S. Thiery, N. Ben Khalifa, Geometrical accuracy in two-stage incremental sheet forming with active medium, in: Production at the Leading Edge of Technology: Proceedings of the 11th Congress of the German Academic Association for Production Technology (WGP), Dresden, September 2021, Springer, 2022, pp. 65–74.

[37] Y. Zimeng, L. Xiaoming, W. Shenli, L. Ling, B. Lang, Effect of isostatic pressing support on forming force in single point incremental forming, Integrated Ferroelectrics 236 (2023) 150–163.

[38] M. Shang, Y. Li, K. Chen, M. Yang, X. Zhao, K. Nie, Incremental forming of hydraulic supports: a numerical and experimental study of thickness distribution, Journal of Mechanical Science and Technology 37 (2023) 6477–6491.

[39] M. Shang, Y. Li, M. Yang, Y. Chen, L. Bai, P. Li, Wall thickness uniformity in isf of hydraulic support: system design, finite element analysis and experimental verification, Machines 11

(2023) 353.

[40] Y. Kumar, S. Kumar, Analysis of incremental sheet forming process through simulation, Int. J. Mech. Prod. Eng. Res. Dev 8 (2018) 145–152.

[41] R. P. Singh, S. Kumar, P. K. Singh, M. Meraz, S. Salunkhe, Advancements in robot-assisted incremental sheet hydroforming: a comparative analysis of formability, mechanical properties, and surface finish for rhomboidal and conical frustums, International Journal of Intelligent Robotics and Applications (2024) 1–13.

[42] R. P. Singh, S. K. Gupta, P. K. Singh, S. Kumar, Robot assisted incremental sheet forming of al6061 under static pressure: Preliminary study of thickness distribution within the deformation region, Materials Today: Proceedings 47 (2021) 2737–2741.

[43] M. Silva, M. Skjødt, P. A. Martins, N. Bay, Revisiting the fundamentals of single point incremental forming by means of membrane analysis, International Journal of Machine Tools and Manufacture 48 (2008) 73–83.

[44] J. Jeswiet, F. Micari, G. Hirt, A. Bramley, J. Duflou, J. Allwood, Asymmetric single point incremental forming of sheet metal, CIRP annals 54 (2005) 88–114.

[45] L. Filice, L. Fratini, F. Micari, Analysis of material formability in incremental forming, CIRP Annals 51 (2002) 199–202.

[46] A. L. Gurson, Continuum theory of ductile rupture by void nucleation and growth: Part i—yield criteria and flow rules for porous ductile media, J. Eng. Mater. Technol. 99 (1977) 2–15. doi:10.1115/1.3443401.

[47] V. Tvergaard, A. Needleman, Analysis of the cup-cone fracture in a round tensile bar, Acta metallurgica 32 (1984) 157–169.

[48] A. H. Naronikar, H. A. Jamadagni, A. Simha, B. Saikiran, Optimizing the heat treatment parameters of al-6061 required for better formability, Materials Today: Proceedings 5 (2018) 24240–24247.

[49] D. Banabic, L. Lazarescu, L. Paraianu, I. Ciobanu, I. Nicodim, D. Comsa, Development of a new procedure for the experimental determination of the forming limit curves, CIRP Annals 62 (2013) 255–258.

[50] S. Taylor, I. Masters, Z. Li, H. R. Kotadia, Comparison of formability and microstructural evolution of c106 copper and 316l stainless steel, JOM 71 (2019) 2721–2727.

[51] M. A. Sutton, J. J. Orteu, H. Schreier, Image correlation for shape, motion and deformation measurements: basic concepts, theory and applications, Springer Science & Business Media, 2009.

[52] S. HAZRA, S. DHARA, S. TAYLOR, Ł. FIGIEL, The non-proportional loading of mild steel, Materials Research Proceedings 41 (2024).

[53] F. A. McClintock, A criterion for ductile fracture by the growth of holes, Journal of Applied Mechanics 35 (1968) 363–371.

[54] J. Rice, D. M. Tracey, On the ductile enlargement of voids in triaxial stress fields, Journal of the Mechanics and Physics of Solids 17 (1969) 201–217.

[55] S. Gatea, H. Ou, B. Lu, G. McCartney, Modelling of ductile fracture in single point incremental forming using a modified gtn model, Engineering Fracture Mechanics 186 (2017) 59–79.

[56] I. French, P. Weinrich, The effects of hydrostatic pressure on the mechanism of tensile fracture of aluminum, Metallurgical Transactions A 6 (1975) 1165–1169.

[57] D. Liu, M. Manoharan, J. Lewandowski, Effects of microstructure of the behavior of an aluminum alloy and an aluminum matrix composite tested under low levels of superimposed hydrostatic pressure, Metallurgical Transactions A 20 (1989) 2409–2417.

[58] M. Yajima, M. Ishii, M. Kobayashi, The effects of hydrostatic pressure on the ductility of metals and alloys, International Journal of Fracture Mechanics 6 (1970) 139–150.

[59] S. Keeler, Forming limit criteria—sheets, in: Advances in deformation processing, Springer, 1978, pp. 127–157.

[60] F. Ozturk, M. Dilmec, M. Turkoz, R. E. Ece, H. S. Halkaci, Grid marking and measurement methods for sheet metal formability, in: 5th International Conference and Exhibition on Design and Production of MACHINES and DIES/MOLDS, 2009, pp. 18–21.

[61] G. Ambrogio, L. Filice, F. Gagliardi, F. Micari, Sheet thinning prediction in single point incremental forming, Advanced materials research 6 (2005) 479–486.

[62] D. Young, J. Jeswiet, Wall thickness variations in single-point incremental forming, Proceedings of the Institution of Mechanical Engineers, Part B: Journal of Engineering Manufacture 218 (2004) 1453–1459.

[63] Y. Jeong, G. Shin, C. Woong, J. H. Kim, J. Yoon, Dissimilar materials welding with a standoff-free vaporizing foil actuator between trip 1180 steel sheets and AA5052 alloy, Materials 14 (2021) 4969.

[64] H. Wu, G. Fan, An overview of tailoring strain delocalization for strength-ductility synergy, Progress in Materials Science 113 (2020) 100675.

[65] M. Kleiner, R. Krux, W. Homberg, Analysis of residual stresses in high-pressure sheet metal forming, CIRP Annals 53 (2004) 211–214.

[66] A. Kumar, R. K. Digavalli, V. Gautam, H. Krishnaswamy, Characterization of residual stresses in conventional forming and hydroforming of tailor welded blanks, Journal of Materials Engineering and Performance 31 (2022) 10171–10186.

[67] M. Fitzpatrick, A. Fry, P. Holdway, F. Kandil, J. Shackleton, L. Suominen, Measurement good practice guide no. 52, Determination of residual stresses by X-ray diffraction (2005) 1–68.

[68] A. Kumar, H. Mehtani, A. Shrivastava, S. Mishra, K. Narasimhan, I. Samajdar, Failure mechanism during incremental sheet forming of a commercial purity aluminum alloy, Engineering Failure Analysis 146 (2023) 107090.

[69] J.-c. Li, F.-f. Yang, Z.-q. Zhou, Thickness distribution of multi-stage incremental forming with different forming stages and angle intervals, Journal of Central South University 22 (2015) 842–848.

[70] B. Bay, N. Hansen, D. Kuhlmann-Wilsdorf, Deformation structures in lightly rolled pure aluminium, Materials Science and Engineering: A 113 (1989) 385–397.

[71] Z. Chang, M. Yang, J. Chen, Experimental investigations on deformation characteristics in microstructure level during incremental forming of AA5052 sheet, Journal of Materials Processing Technology 291 (2021) 117006.

[72] A. Kumar, A. Shrivastava, K. Narasimhan, S. Mishra, Microstructure and texture evolution during incremental sheet forming of AA1050 alloy, Journal of Materials Science 57 (2022) 6385–6398.

[73] K. G. Schell, F. Lemke, E. C. Bucharsky, A. Hintennach, M. Hoffmann, Microstructure and mechanical properties of li 0.33 la 0.567 tio 3, Journal of Materials Science 52 (2017) 2232–2240.

[74] Q. Gao, H. Zhang, H. Li, X. Zhang, F. Qu, Y. Jiang, Z. Liu, C. Jiang, Hot deformation of alumina-forming austenitic steel: Ebsd study and flow behavior, Journal of Materials Science 54 (2019) 8760–8777.

[75] M. Winning, A. D. Rollett, Transition between low and high angle grain boundaries, Acta materialia 53 (2005) 2901–2907.